Accepted Manuscript

Metallogenesis at the Carris W-Mo-Sn deposit (Gerês, Portugal): Constraints from fluid inclusions, mineral geochemistry, Re-Os and He-Ar isotopes

A. Moura, A. Dória, A.M.R. Neiva, C. Leal Gomes, R.A. Creaser

PII: S0169-1368(13)00168-6
DOI: doi: 10.1016/j.oregeorev.2013.08.001
Reference: OREGEO 1074

To appear in: *Ore Geology Reviews*

Received date: 22 March 2012
Revised date: 8 August 2013
Accepted date: 9 August 2013

Please cite this article as: Moura, A., Dória, A., Neiva, A.M.R., Gomes, C. Leal, Creaser, R.A., Metallogenesis at the Carris W-Mo-Sn deposit (Gerês, Portugal): Constraints from fluid inclusions, mineral geochemistry, Re-Os and He-Ar isotopes, *Ore Geology Reviews* (2013), doi: 10.1016/j.oregeorev.2013.08.001

Metallogenesis at the Carris W-Mo-Sn deposit (Gerês, Portugal): constraints from fluid inclusions, mineral geochemistry, Re-Os and He-Ar isotopes

A. Moura[a*], A. Dória[a], A.M.R. Neiva[b], C. Leal Gomes[c], R.A. Creaser[d]

a. Departamento de Geociências, Ambiente e Ordenamento do Território, Faculdade de Ciências, Universidade do Porto and Centro de Geologia da Universidade do Porto (CGUP). Rua do Campo Alegre, 687, 4099-007 Porto, Portugal

b. Departamento de Ciências da Terra e Centro de Geociências, Universidade de Coimbra, 3000-272 Coimbra, Portugal.

c. Escola de Ciências, Departamento de Ciências da Terra, Centro de Investigação Geológica, Universidade do Minho, Gualtar – 4710-057 Braga, Portugal.

d. Department of Earth and Atmospheric Sciences, University of Alberta, 126ESB, Edmonton, AB Canada T6G2R3.

Abstract

The Carris orebody consists of two partially exploited W-Mo-Sn quartz veins formed during successive shear stages and multipulse fluid fillings. They cut the Variscan post-D3 Gerês I-type granite. The most important ore minerals are wolframite, scheelite, molybdenite and cassiterite. There are two generations of wolframite. The earlier generation of wolframite is rare and has the highest WO_4Mn content (91 mol%) and the most common wolframite contains 26-57 mol% WO_4Mn. Re-Os dating of molybdenite from the ore quartz veins and surrounding granite yield ages of 279 ±1.2 Ma and 280.3±1.2 Ma, respectively which are in very good agreement with the previous ID-TIMS U-Pb zircon age for the Carris granite (280±5 Ma).

$^{3}He/^{4}He$ ratio of pyrite ranging between 0.73 and 2.71 *Ra* (1 *Ra* = $1.39x10^{-6}$) and high $^{3}He/^{36}Ar$ ($0.8\text{-}5x10^{-3}$) indicate a mixture of a crustal radiogenic helium fluid with a mantle derived-fluid.

The fluid inclusion studies on quartz intergrown with wolframite and scheelite, beryl and fluorite reveal that two distinct fluid types were involved in the genesis of this deposit. The first was a low to medium salinity aqueous carbonic fluid (CO_2 between 4-14 mol%) with less than 1.95 mol% N_2, which was only found in quartz associated with wolframite. The other was a low salinity aqueous fluid found in all the four minerals. The homogenization temperatures indicate minimum entrapment temperatures of 226-310ºC (average 280ºC) for the $H_2O\text{-}CO_2\text{-}N_2\text{-}NaCl$ fluid and averages temperatures of 266ºC for scheelite and 242ºC, 190ºC and 160ºC for the last generations of beryl, fluorite and quartz, respectively. It was estimated that wolframite was deposited ~7 km depth, assuming a lithostatic pressure, probably due to strong pressure fluctuation caused by seismic events triggered by brittle tectonics during the exhumation event. Precipitation of scheelite and sulphides took place later, at the same depth, but under an hydrostatic or suprahydrostatic pressure regime, and probably caused by mixing between the magmatic-hydrothermal fluid and meteoric waters that deeply penetrated the basement during post-Variscan decompression.

---

* Phone: (+351) 220 402 458, E-mail: ajmoura@fc.up.pt

Keywords: Carris; tungsten; Portugal; geochemistry; fluid inclusions; Re-Os and He-Ar isotopes

1. Introduction

Tungsten, tin and molybdenum are three important metals for many applications of everyday life products. Production of tungsten and molybdenum in 2010 was the highest ever. Since 2003 prices of tungsten and tin concentrates were multiplied by five, and by three for molybdenum, which attest the present economic importance of these metals.

Portugal is one of the two European tungsten producers and the country has a long tradition of W mining with hundreds of exploitations in the XX century. Between 1900 and the present, the country has produced around 190,000 t of WO_3 concentrate (Moura, 2010). The two main Portuguese W deposits are Panasqueira, an active mine with a production of 1,200 t of WO_3 concentrate in 2010 and Borralha (closed in 1985, due to the decline of W prices), which are World-class deposits. Most Portuguese W deposits consist of W-Sn quartz veins spatially associated with S-type granites (Neiva, 2002), but the W-Mo-Sn Carris orebody is associated with I-granites. All these hydrothermal deposits belong to a metallogenetic Variscan province in the Western Europe, related to post-collision tectonics and magmatism (Štemprok, 1981). This province (Fig. 1) also has a great importance in Spain, Cornwall (Great Britain), Armorican and Central massifs (France), Erzgebirge-Krušné hory (Germany and Czech Republic) and in the northern and central Portugal (Jackson et al., 1989; Marignac and Cuney, 1999; Štemprok and Seltmann, 1994; Vindel et al., 1995).

Ore-forming fluids play an important role during the formation of any hydrothermal ore deposit. Therefore, the characteristics, origin and evolution of ore-forming fluids are important for metallogenic studies. Several mechanisms have been considered for the initiation of wolframite precipitation, such as boiling, fluid mixing, cooling, pressure decrease and wall-rock reactions; this will be referred later in the discussion. Helium and argon are good indicators for decipher the provenience of the hydrothermal fluids in terms of crust-mantle origin. The $^{3}He/^{4}He$ ratio is ~100-1000 times lower in fluids of crustal origin (0.05-0.01 *Ra*) than in fluids from the sub-continental mantle ($0.8\text{-}1x10^{-5}$, or 6-7 *Ra*). This ratio and $^{3}He/^{36}Ar$ values provide information on the origin of ore-forming fluids (e.g. Hu et al., 2012).

This paper presents the geology of the area and Carris orebody, mineralogical features and the mineral paragenesis of veins, fluid inclusions studies (microthermometric and Raman microspectrometry), Re-Os age of molybdenite and He-Ar analyses of fluids from pyrite to identify their origin. Research on the metallogeny of this W deposit is a contribution to the

knowledge of W formation in the European Variscides and particularly in the metallogeny of NW of Iberian Peninsula.

2. Geological setting

The Carris mine is located in northern Portugal in the highest zone of the Gerês Mountain, close to the Spanish border, about 500 m southeast of the Carris geodesic mark. The mine occurs in the Peneda-Gerês Variscan granitic massif that crops out in an area of 40 x 20 km across the border between northern Portugal and Spain (Fig.2A and 2B). This massif belongs to the Central Iberian Zone (CIZ, Fig. 2A), which is one of the main geological zones of the Variscan orogeny in the Western Europe (Julivert et al., 1974; Mattauer and Etchecopar, 1977). The European Variscides are tectonically characterized by a classical obduction-collision belt originated from the convergence, obduction, subduction and collision of the North Laurentia and the Gondwana continents, with minor intermediate blocks (e.g. Dias and Ribeiro, 1995; Mendes and Dias, 2004). In the CIZ, large volumes of granitoids were emplaced during the post-collisional stage of the Variscan orogeny (syn- to post-D3 related to post-thickening extensional tectonics, e.g. Ferreira et al., 1987). The Peneda-Gerês massif is a post-D3 composite and zoned batholith spatially associated with the NNE fault of Gerês-Lovios. It is composed of several granite facies (Mendes, 2001; Mendes and Dias, 2004). The coarse- to medium-grained porphyritic light pink biotite granite is the most the extensive facies, dated 296±2 Ma by ID-TIMS U-Pb of monazite (Dias et al., 1998) and hosts the W-Mo-Sn quartz veins from Carris (Fig. 2B). The fine-grained slightly porphyritic biotite Carris granite crops out in the Gerês granite as several hectometric irregular masses. The Carris orebody is hosted in both granites (Fig. 3). A ID-TIMS U-Pb zircon age for the Carris granite is 280±5 Ma, taken as a minimum emplacement granite age (Dias et al., 1998). Both granites intruded Silurian metasediments and syn- and late-D3 granites (Fig. 2B). They are I-type granites (Neiva, 1993) and result from mantle input followed by mantle-crust interactions (Neiva, 1993; Mendes and Dias, 2004). The Carris mine is located on an alignment that trends NNW-SSE where three

other old mines Las Sombras (1.5 km to the north, in Spain), Borrageiro (4 km to the south) and Borralha (15 km south of Borrageiro) of similar type and paragenesis occur (Fig.2B). Hectometric bands of episyenitic rocks occur in many parts of the Peneda-Gerês massif. Episyenites result from significant petrographic and chemical changes of granites. The former include dissolution of quartz, occurrence of red microcline with a high triclinicity, albitization of feldspars, total alteration of biotite into chlorite and significant amounts of pistacite and hematite. The latter consist of a strong loss of SiO_2 content, decrease of Ba and Rb contents and increase of Al_2O_3 and Na_2O contents (e.g. Jaques, 2008) and decrease of volume. Episyenites are interpreted as a result of high pressure fluids generated after the intrusion of the granite and before the formation of W quartz veins (Cheilletz and Giuliani, 1982). The K-Ar age of K-feldspar from episyenites derived from the alteration of the Gerês granite is 273.6±11.7 Ma (Jaques, 2008). Episyenitization of this granite occurred after the W-mine and is mainly due to changes in the fluid composition towards a more alkaline aqueous fluid of meteoric origin (Jaques et al., 2010). However important episyenite bands are not close to the mineralized quartz veins from Carris for hundreds of meters (Cheilletz and Giuliani, 1982).

3. The Carris orebody

The Carris mine was a tungsten producer between 1943 and 1979. During this period the mine produced more than 1,000 t of wolframite concentrate and subordinate amounts of molybdenite concentrate (56 t, mainly in the period 1952-58; Moura, 2010) and even smaller cassiterite concentrates. It was the only producing molybdenite mine in Portugal. The Carris exploitation began in 1943 with the mining of the W-rich coluvial placers and also underground. Mining reached the 155 m below surface in seven levels and ended in 1974. The fifth level was the longest up to 500 m. A total of 2 500 m of galleries were in production and most of the 62,000 t of estimated ore (Mills and Fine, 1972) are still in place. The average ore grade during exploration was 0.5-0.8 % WO_3, 0.07 % Mo, 0.01 % Sn, 0.025 % Bi and 0.006 % Cu (Weeks, 1979). Based on petrographic observations and mining production we conclude that wolframite

is around 8-9 times more abundant than scheelite and about 6-10 times more abundant than molybdenite. The Carris main deposit consists of three quartz vein systems running N-S (Fig. 3). The Salto do Lobo vein is approximately 25-30 m east of the Paulino vein and the third vein is approximately 75-80 m east of the Salto do Lobo vein. In general, all three veins dip to the east about 85º. However Salto do Lobo vein is sinuous and reverses to the west below 130 m from the surface. Paulino and Salto do Lobo veins are bordered on the east by a strong fault parallel to the Salto do Lobo vein about 15 m to the east. The fault is 20-40 cm wide and dips 80-85º to the west. The fault crosses the Salto do Lobo vein near the main hosting shaft and offsets the vein laterally and downthrow (Mills and Fine, 1972). The average set of mineralized stringers of quartz is usually 2 m wide but varies between 1 to 3 m. The stringer varies in width from 5 cm up to 20 cm. In the richest ore-shoots there are usually 2 stringers at least 6 cm wide that carry the majority of the ore. The number of stringers in a system usually are 5-8 but there are as many as 15 (Mills and Fine, 1972). These strings correspond to quartz infilling in dilation sites associated with shear. The inner structure of shear corridors shows a rupture geometry and quartz-filling textures compatible with pure extensive or transpressive to transtensive deformation (Fig. 4).

4. Sampling and analytical methods

Samples were mainly collected underground, particularly in the accessible levels 1 and 2 (old mining drawings, 1953) of the Carris mine, but samples from this mine belonging to the collection of the Centro de Geologia, Universidade do Porto (CGUP) were also studied.

All minerals were analyzed for major and trace elements and backscattered images were obtained using a Hyperprobe JEOL JXA-8500F electron microprobe at the National Laboratory of Energy and Geology, S. Mamede de Infesta, Portugal. Standards used include albite (Na Kα), orthoclase (Al Kα, Si Kα, K Kα), apatite (Ca Kα), MgO (Mg Kα), $MnTiO_3$ (Mn Kα), TiO_2 (Ti Kα), Fe_2O_3 (Fe Kα), ZnS (Zn Kα) fluorite (F Kα), $BaSO_4$ (Ba Lα), $SrTiO_3$ (Sr Lα), glass Ge-Al-Ca containing 10.0 wt% Rb (Rb Lα) and Si-Al-Ca with 10.0 wt% Cs (Cs Lα), cassiterite (Sn

Kα), pure Ta (Lα), Mo (Lα), Ni (Kα), Co (Kα), Cu (Kα), Ag (Lα) and Au (Mα) metals, $SrBaNbO_4O_{12}$ (Nb Lα), scheelite (W Lα), Sc_2O_3 (Sc Lα), UO_2 (U Mβ), ThO_2 (Th Mβ), galena (Pb Mα), LaP_5O_{14} (La Lα), CeP_5O_{14} (Ce Lα), YAg (Y Lα), Cd (Lα), Sb_2S_3 (Sb Lα), AsGa (As Lα), Bi_2Se_3 (Bi Mα). But pyrite (Fe Kα, S Kα) was used for sulphides and sulphosalt.

Analyses of silicates and oxides (cassiterite, rutile, ilmenite and ixiolite) were conducted at an accelerating voltage of 15 kV and a beam current of 10 nA, but those of uraninite, wolframite, scheelite, zavaritskite, sulphides and sulphosalt at 20 kV and 20 nA. Each element was counted for 20s, except ZnO, BaO, Rb_2O, Cs_2O and F from silicates for 80 s and ZAF corrections were applied. Detection limits (3σ) above mean background were < 0.03 wt% oxide of silicates and oxides, except for ZnO, BaO, Rb_2O and Cs_2O (0.06 wt.%) and F (0.1 wt.%).

Petrography, microthermometry and Raman analyses of fluid inclusions have been carried out at the laboratories of the Centro de Geologia da Universidade do Porto (CGUP), in doubly-polished wafers of about 150-200 μm thickness. Microthermometric characterization of the fluids was performed using a Chaixmeca heating-freezing stage (Poty et al., 1976) for cryometric analyses, and a Linkam THMSG 600 stage (Shepherd, 1981) for the thermometric studies. Calibration was carried out with natural and synthetic fluid inclusions standards at T≤0ºC and with melting-point standards at T>25ºC. The accuracy was ±0.1 °C during cryometric measurements and ±1 °C during heating. Volumetric proportions between volatile and aqueous phases were estimated optically at room temperature by reference to volumetric charts. Molar fractions of CO_2 and N_2 were determined by Raman microspectroscopy analyses in selected individual inclusions using a Labram Dilor-Jobin Yvon Spectrometer attached to an Olympus microscope. The excitation source was a He–Ne laser with 632.8 nm wavelength operated at 20 mW. Measurement of the N_2 signal from the air was done immediately after each fluid inclusion analysis. The quantification of the different species in the inclusions was obtained using a computer program developed at CGUP that follows routine procedures described by Prieto et al. (2012). Salinity (expressed as equivalent wt% of NaCl) of the aqueous inclusions was calculated from microthermometric data using the revised equation of Bodnar

(1993). Bulk composition of both types of fluids was calculated using Bakker (2003) codes. Isochores for the aqueous carbonic fluids were calculated using Bakker (2003) software based on Bakker (1999) and Bowers and Helgeson (1983) equations of state. The isochores for the H_2O-NaCl inclusions were calculated from the equation of state of Knight and Bodnar (1989).

The material analyzed for Re-Os isotopes consists of two samples containing molybdenite in the Salto do Lobo vein (PV1) and from the Gerês granite (PG1) outcropping near the mine. Molybdenite was obtained by metal-free crushing of the samples, followed by gravity and magnetic concentration methods, to obtain a pure mineral separate. Methods used for molybdenite analysis are described in detail by Selby and Creaser (2004). The ^{187}Re and ^{187}Os concentrations in molybdenite were determined by isotope dilution mass spectrometry using Carius-tube, solvent extraction, anion chromatography and negative thermal ionization mass spectrometry techniques. For this work, a mixed double spike containing known amounts of isotopically enriched ^{185}Re, ^{190}Os, and ^{188}Os analysis was used (Markey et al., 2007). Isotopic analysis used a ThermoScientific Triton mass spectrometer by Faraday collector (Re) or SEM (Os). Total procedural blanks for Re and Os are less than <2 picograms and <3 picograms, respectively. These procedural blanks are insignificant in comparison to the Re and Os concentrations in molybdenite. The Chinese molybdenite powder HLP-5 (Markey et al., 1998) is routinely analyzed at the University of Alberta, and during the period of analysis of the PV1 and PG1 samples returned a Re-Os date of 221.5 ± 0.9 Ma identical to that reported by Markey et al. (1998) of 221.0 ± 1.0 Ma. In addition, the age determined for the Henderson Molybdenite Reference Material RM8599, using the above methods and instrumentation, was 27.71 ± 0.13 Ma, in accord with previous determinations (Markey et al., 2007).

Pyrite samples for He-Ar isotopes were collected in W-Mo-Sn ores from level 1 (old mining drawings, 1953). After the samples were crushed, mineral chips were hand-picked under a binocular microscope. An all metal extraction line and mass spectrometer (GV 5400) at the Institute of Geochemistry, Chinese Academy of Sciences, Guiyang, was used following the procedure given by Hu et al. (2012). Approximately 500-1,000 mg of separated coarse

(generally 0.5~1.5 mm, but the coarser the better) pyrite grains were cleaned ultrasonically in alcohol, dried, then loaded in on-line in vacuo crusher buckets. The samples were baked at ca.150°C on-lined with the ultra-high vacuum system for >24 h prior to analysis in order to remove adhered atmospheric gases. Gases were released from the grains into the all metal extraction system by sequential crushing in modified Nupro type valves. The released gases were exposed to a titanium sponge furnace at 800°C for 20 minutes to remove the bulk of active gases (e.g. H_2O and CO_2), and then exposed to two SAES Zr-Al getters (one at room temperature, the other at 450°C) for 10 min to further purify. He was separated from Ar using an activated charcoal cold finger at liquid N_2 temperature (−196°C) for 40–60 minutes to trap Ar. He and then Ar isotopes and abundances were analyzed on the GV 5400. Gas abundances were measured by peak-height comparison with known amounts of standard air from an air bottle. He and Ar abundances and isotopic ratios were calibrated against pipettes of 0.1 cm^3 STP air ($5.2\times10-7$ cm^3 STP 4He and $9.3\times10-4$ cm^3 STP 40Ar). Procedural blanks were $<2\times10-10cm^3$ STP ^{4}He and $(2\sim4)\times10-10cm^3$ STP ^{40}Ar, and constituted <1% of analyses. The blank is too low to affect calibration of the abundance measurement.

5. Mineralogical characteristics of tungsten-molybdenum-tin quartz veins

The mineralogical characteristics and relative abundance of minerals in the W-Mo-Sn quartz veins from Carris are given in Table 1. The distinct paragenesis observed in well-delimited veins are sequenced according to successive episodes of shear, which are responsible for the crack-seal inner structure due to recurrent fracture and quartz sealing containing Be, Nb, Ta, Sn, Mo, W, Bi, Zn and Cu mineralization (Fig. 4 – stages 3 to 6).

In earlier paragenetic stages, potassic phyllitic, microcline, hematite or albite, chlorite and sulphide hydrothermal alteration occurs and also feldspar selvages with comb structure. The peripheric comb growing of some alkali feldspar crystals from the quartz veins is concordant with the inner stretching of some vein minerals, passing gradually to a microcline plus quartz association with a graphic pegmatitic texture at the border. The microcline selvages and feldspar

borders observed in some quartz veins mark a typical and gradual transition between the generation of miarolitic pegmatites and the precipitation of hydrothermal quartz, both focused in the same structures during successive shear stages and multipulse fluid fillings.

The pegmatite assemblages are typical of the early stages of mineralization and are important for the Sn enrichment, as the Sn content increases from parent granite to pegmatite by fractional crystallization (e.g. Neiva and Ramos, 2010). Most of the pegmatites present a concordant orientation with the mineralized quartz veins and consequently are syntaxial relatively to shear (Fig. 4 – stage 3). In other places, younger pegmatites show orthogonal orientation and inner crystal-growth relatively to the hydrothermal veins and are antitaxial relatively to the shear (Fig. 4 – stages 1 to 3). The antitaxial and syntaxial pegmatites are cogenetic and paragenetically belong to the rare element class and NYF type.

Paragenetic analysis reveals a sequential crystallization between pegmatite assemblages, quartz fillings of the dilatational porosity and hydrothermal alteration of the host granite suggesting a generalized syn-kinematic character relatively to shear. One of the best examples is given by the occurrence of blue Fe beryl crystals associated with euclase in the transition of the intermediate zone to the quartz core of pegmatites. It also occurs disseminated in the host granite affected by the hydrothermal alteration associated with the tungsten mineralization (Fig. 5).

Under the microscope the quartz associated with wolframite is slightly milky and of millimetric to submillimetric dimension; generally has low deformation features such as ondulating extinction and subgrains. Three generations of fluorite occur. The first was observed within miarolitic cavities in the pegmatite facies. In quartz veins, the earlier fluorite crystals are unzoned and the later fluorite crystals are complexely zoned in BSE images (Fig. 6a, g). Backscattered electron images (BSE) combined with quantitative spot electron microprobe analyses made it possible to distinguish six generations of muscovite, which will provide some information on the changes of fluid composition. A few crystals included in albite have a darker core and a lighter rim, but in general muscovite is oscillatory zoned in BSE images (Fig. 6a, b, c). Two generations of chlorite occur. The earlier is unzoned, but a few crystals have a lighter

zone with patches of the darker zone in BSE images, and the latter also partially surrounds the former zone (Fig. 6d). The latter generation is mainly observed filling wolframite II fractures. Two generations of cassiterite occur (Table 1). The earlier subhedral cassiterite (Fig. 6e) shows darker and lighter growth-zones in BSE images, which are narrow mainly parallel alternating in some crystals. A lighter zone in a BSE image corresponds to an optical darker zone. Optically the lighter zones are colourless to tan and translucent, whereas the darker zones are slightly pleochroic from ε brown to ω light brown. The later anhedral cassiterite is unzoned and brown in colour.

Wolframite crystals observed microscopically are dark brown to black in colour. The earlier crystals do not contain inclusions. The most common wolframite consists mainly of crystals without inclusions and in general surrounded by scheelite. The later crystals are partially replaced by scheelite, which penetrated along cleavages (Fig. 6f). Arsenopyrite is the earliest sulphide and presents two generations (Table 1). Some crystals of both generations are zoned in BSE images, mainly oscillatory zoned (Fig. 6j), but others have a darker core and a lighter rim. A few pyrite grains belonging to the earlier generation are lighter in BSE images and rare grains are complexely zoned, showing mainly a darker zone but with a few lighter areas. Molybdenite is the most abundant sulphide. Stannite is zoned, and the lighter zone in BSE images is irregularly distributed, but surrounded by the most common darker zone.

Figure 7 presents four metallographic representative textures of the main ore minerals. The sequence of the mineral paragenesis is presented in Fig. 8.

6. Chemical characteristics of minerals from tungsten- molybdenum-tin quartz veins

6.1. Silicates

Albite and microperthitic microcline are nearly pure (Table 2). In muscovite, the lighter zones in BSE images have higher Ti, Fe^{2+}, Mn, Mg, Li and F contents and lower Al^{VI} and OH contents than the darker zones from the same crystal (Table 3). The lighter zone of muscovite from the first to the fourth generation shows progressive increase in Fe^{2+}, Mg, Li and F contents and

decrease in Al^{VI} and OH contents and the same is observed in the darker zone (Table 3). But Fe^{2+}, Mg, Li and F contents decrease and Al^{VI} and OH contents increase from the darker zone of muscovite 4 surrounding cassiterite (Fig. 6b) to the same zone of muscovite 5 surrounding wolframite and scheelite (Fig. 6c). The same occurs in the lighter zone. However, afterwards for the darker and lighter zones Fe^{2+}, Mg, Li and F contents increase and Al^{VI} and OH contents decrease from muscovite 5 to muscovite 6 surrounding sulphides. Muscovite 2 intergrown with chlorite is unzoned, but also has higher Fe^{2+}, Mg, Li and F contents and lower Al^{VI} and OH contents than the darker zone of muscovite 1 included in albite, but it contains higher Al^{VI}, Mg and OH contents and lower Fe^{2+}, Li and F contents than the lighter zone of this muscovite 1 (Table 3). Both darker and lighter zones of muscovite 3 included in quartz show the normal evolution compared to muscovite 2.

The darker zone in BSE images of chlorite has higher Si, Al^{VI}, Mg contents and lower Fe^{2+} content than the lighter zone (Table 4, Fig. 6d). Most chlorite is unzoned and has a composition, whose Fe^{2+} and Mg contents are between those for darker and lighter zones (Fig. 9). However, an unzoned chlorite occurring at the border of muscovite has a composition similar to that of lighter zone. The chemical composition corresponds to chamosite.

6.2. Oxides

Rutile inclusions occur in muscovite of the first and second generations and cassiterite. In general, they are irregularly zoned, but some are homogeneous. Those included in cassiterite contain Nb>Ta and up to 2.34 wt% SnO_2, 14.14 wt% Nb_2O_5, 12.85 wt % Ta_2O_5, 0.26 wt% WO_3, 6.87 wt% FeO and 0.06 wt% MnO and have higher Nb, Ta, Sn and Fe contents and lower Ti content than rutile included in muscovite (Table 5). The incorporations of Sn and W in rutile will be by the substitutions $Sn^{4+} \leftrightarrows Ti^{4+}$ and $W^{6+}\ Fe^{2+} \leftrightarrows 2Ti^{4+}$ (Neiva, 1996). The incorporations of Nb, Ta and Fe^{2+} in rutile may be explained by the substitution $2(Nb, Ta)^{5+} + Fe^{2+} \leftrightarrows 3Ti^{4+}$, but some deviation from this substitution may eventually be caused by $Fe^{3+}(Nb, Ta)O_4$. Inclusions of ilmenite occur in cassiterite (Table 5) and contain up to 3.63 wt% MnO. Some are homogeneous and others are irregularly zoned.

There is no significant chemical distinction between darker and lighter zones, in a BSE image (Fig. 6e) of the earlier generation of cassiterite. A representative composition is given in Table 5 for both zones. Cassiterite is nearly pure, containing up to 0.16 wt% Nb_2O_5, 0.22 wt% Ta_2O_5, 0.67 wt% TiO_2, 0.97 wt% WO_3, 0.27 wt% FeO and 0.06 wt% MnO. The younger generation of cassiterite is pure, containing only 0.14 wt% FeO (Table 5).

Very rare ixiolite is included in wolframite and scheelite. Some crystals are homogenous and others heterogeneous, and up to 104x45 μm. Their compositions belong to the ixiolite-wodginite family in the diagrams Ta^{5+} versus Nb^{5+} and (Nb+Ta)-(Fe+Mn)-(Sn+Ti+W) (Neiva, 1996). They contain up to 3.83 wt% TiO_2, 2.01 wt% SnO_2, 19.09 wt% WO_3 and 6.46 wt% Sc_2O_3. The richest composition in Sn, W and Sc is given in Table 5. In general, ixiolite contains Nb>Ta, Sc>W>Ti>Sn, but occasionally it has Sc>Ti>W>Sn.

The earliest crystals of wolframite have 91 mol% WO_4Mn. The most common wolframite contains 26-57 mol% WO_4Mn. However, the composition within each crystal is homogeneous with a difference of less than 4 mol% WO_4Mn. The youngest crystals have 27-30 mol% WO_4Mn, being within the range of the most common wolframite. There is a gap between the two main compositions of wolframite (Fig. 10a), suggesting that they are derived from fluids with at least slightly distinct composition. The Nb_2O_5 content is significant in the most common wolframite, ranging from 0 to 4.93 wt%. This is the highest Nb content found in Portuguese wolframite (Neiva, 2008) and occurs in wolframite from Carris with 26 mol% WO_4Mn (Table 5). The Fe^{3+} and Fe^{2+} contents were calculated on the basis of a charge balance of 2 cations. The Nb content tends to correlate negatively with W. The strong negative correlation between $(W^{6+}+Fe^{2+}_{cal}+Mn^{2+})$ and $(Nb^{5+}+Fe^{3+}_{cal})$ (Fig. 10b) suggests the coupled substitution $[(Fe, Mn)^{2+}+ W^{6+}] \leftrightarrows (Fe^{3+}+ Nb^{5+})$ which was also found for wolframite from other Portuguese deposits (Neiva, 2008).

Scheelite is homogeneous and fairly pure containing up to 0.15 wt% MoO_3 (Table 5). Uraninite shows an homogeneous composition (Table 5).

6.3. Sulphides

The sulphide compositions are given in Table 6. The arsenopyrite is As-deficient and S-rich. In the zoned crystals (Fig. 6j), the lighter zone in BSE images has a higher As content and a lower S content than the darker zone (Fig. 11a, b). Therefore, the oscillatory zoned crystals present irregular behaviours of As and S contents, whereas in other zoned crystals As content increases and S content decreases from core to rim (Table 6). There is no chemical distinction between early and late arsenopyrite chemical compositions ranging from below 28 to above 30 percent As (Fig. 11c). The Au content of arsenopyrite is up to 0.15 wt.%, which is close to that of arsenopyrite from Portuguese gold quartz veins (Neiva, 1994; Neiva et al., 2008). The Au content of arsenopyrite is not correlated with As content and gold probably occurs as sub-microscopic inclusions of native gold (e.g. Cook and Chryssoulis, 1990).

In general, no chemical distinction was found between the two generations of pyrite. A few grains of the earlier generation and lighter areas in BSE images of zoned crystals have higher As content and lower S content than the common pyrite grains (Fig. 11d). The Au content of pyrite is up to 0.11 wt% and very close to that of pyrite from Portuguese gold quartz veins (Neiva, 1994; Neiva et al., 2008). The richest pyrite in Au is not the richest in As and As may facilitate incorporation of Au into the pyrite structure (Cooke and Chryssoulis, 1990). The Au content of pyrite does not correlate with any other element and therefore the elevated Au concentrations are attributed to very small inclusions of gold.

In general, cosalite shows compositions of $(Pb_{1.80}\ Ag_{0.18}\ Cu_{0.06})_{\Sigma 2.04}\ (Bi_{2.06}\ Sb_{0.09})_{\Sigma 2.15}\ S_5$, but it contains up to 3.12 wt% Ag. Galena has an homogeneous composition, containing up to 0.36 wt% Ag (Table 6). The FeS mol% of the analysed sphalerite ranges between 10.1 and 17.6 (Table 6). In a few individual sphalerite grains, mol% FeS content increases from core to rim from 10.1 up to 14.0. Sphalerite does not contain Cu, but diffusion-induced segregations of chalcopyrite (e.g. Bente and Doering, 1993) occur. Chalcopyrite has an homogeneous composition (Table 8). Molybdenite is pure and bismuthinite contains up to 0.49 wt% Sb (Table 6). In stannite, the lighter zone has a higher Ag content and lower Cu, Zn and Sn contents than

the darker zone (Table 6). The kesterite composition $Cu_{2.09}$ $(Zn_{0.55}\,Fe^{2+}_{0.42}\,Mn_{0.01})_{\Sigma 0.98}$ $Sn_{0.98}S_4$ has some Fe^{2+} and is ferrokesterite.

6.4. Halides

In the second generation of fluorite, the lighter zone in BSE images has a higher F content than the darker zone. The unzoned crystals of the first generation of fluorite have a composition close to the lighter zone (Table 7) of the zoned crystals. The zavaritskite (Fig. 6i) has a composition of $Bi_{1.01}\,OF_{0.97}$ (Table 7).

6.5. Element

Native bismuth is nearly pure containing up to 0.87 wt% Sb (Table 7).

7. Fluid inclusion studies

Studies of the types and petrography of fluid inclusions were carried out on wafers from representative samples of the Salto do Lobo vein. The succession of fluids and possible mineralization events has been studied by interpreting the relationships between fluid inclusions and the different host minerals. The fluid inclusion studies were performed in quartz related to wolframite, and in scheelite, the later beryl and the later fluorite (Fig. 12). The fluid inclusion studies were focused on fluid inclusion assemblages composed of groups of inclusions, isolated inclusions or inclusions in trails, all with identical characteristics concerning the vapor/liquid ratio, composition, heating and freezing behavior. The lack of growth zones in the studied minerals preclude an undoubtable classification as primary inclusions and according to Roedder (1984) at least some of the isolated inclusions may be primary in origin. The textural relationship of the quartz and other fluid inclusion-bearing minerals with the ore minerals was particularly important to the interpretation.

7.1. Fluid characterization

From petrographic, microthermometric and Raman characteristics two types of fluids were recognized: (i) aqueous carbonic fluids (H_2O-CO_2-N_2-NaCl) and, (ii) low salinity aqueous fluids (H_2O-NaCl). All the studied fluid inclusions are between 5 and 25 μm. The aqueous carbonic fluids were observed in clusters, occasionally isolated and in intragranular trails only in quartz associated with the earliest wolframite placed a few micron from this mineral. A summary of the microthermometric, micro-Raman data and bulk composition is given in Tables 8 and 9.

7.1.1. Aqueous carbonic fluids

These inclusions (designated Lc-w) are three-phase at room temperature and have an average degree of filling of 0.7-0.8. The melting temperature of the CO_2 phase was observed between -58.3 and -57.0ºC, the melting temperature of clathrate is in the range +7.2 to +10.1ºC and the CO_2 homogenization temperature was observed in the range of 21.4 to 25.5ºC (into liquid) and 23.0 to 26.1ºC (into vapour). Flc (liquid CO_2/total CO_2) are between 0.50 and 0.80. The total homogenization temperatures (Th) in these fluid inclusions were observed between 276 and 310ºC (mode between 280-290ºC) to the liquid phase, except one Th at 226ºC (Fig. 13). Many of the Lc-w inclusions decrepitated during heating experiments.

A representative set of these inclusions was selected for Raman spectroscopy analyses. The only gases species found were carbon dioxide (CO_2) and nitrogen (N_2). CO_2 is the dominant species in the volatile phase (Fig. 15) ranging from 84.3 to 98.0 mole %, and N_2 content ranges from 2.0 to 15.7 mole %. These fluids have the following bulk compositions (%): 92.70-77.38 H_2O, 14.74-4.22 CO_2, 1.92-0.05 N_2 and 5.25-0.04 Na^+ and the same for Cl^-. The densities are between 0.94 and 0.72 gcm^{-3} (Table 9).

7.1.2 Aqueous fluids

This type of fluid was trapped as fluid inclusions (Lw) in quartz associated with wolframite, scheelite, fluorite III and beryl III (Fig. 8). Lw inclusions are two-phases water-rich inclusions with a degree of filling (Flw) varying from 0.70 to 0.90. The scheelite aqueous fluid inclusions

occur as isolated individual or groups. The fluid inclusions in beryl and fluorite are found in intracrystalline alignment possibly along cleavages. Fluid inclusions in quartz associated with wolframite II are mainly found in trails of possible secondary origin (Fig. 12). Ice melting temperatures (Tm_{ice}) of Lw fluid inclusions observed in quartz lie between -7.4 and -0,1ºC (average of -3.4ºC) which corresponds to salinities of 11.0-0.2 eq. wt.% NaCl (average of 5.6 eq. wt. % NaCl). Fluid inclusions in scheelite show Tm_{ice} between -5.0 and -0.9 ºC with an average of -4.0ºC corresponding to salinities between 1.6 and 7.9 eq. wt.% NaCl (average of 6.4 eq. wt.% NaCl). The fluid inclusions in fluorite show Tm_{ice} ranging from -0.9 to -0.1ºC (average of -0.5ºC) corresponding to an average of 0.9 eq.wt.% NaCl and between -3.7 and -0.1ºC of fluid inclusions in beryl, with an average of -1.9ºC, which corresponds to salinities of 6.0-0.2 eq. wt. % NaCl (average of 3.4 eq.wt. % NaCl). In this type of fluid inclusions, the total homogenization (Fig. 13 and 14) occurs always in the liquid phase. Lw inclusions in scheelite display Th between 230 and 281ºC (average of 266ºC); inclusions in beryl show Th between 235 e 250ºC; in fluorite the inclusions display a large range of Th between 143 e 306ºC (average of 200ºC) and in quartz Lw inclusions are characterized by Th values between 130 and 230ºC (average of 178ºC). The densities are between 0.84 and 0.99 gcm^{-3}.

According to Thomas et al., 2011, 2012; Sun and Qin, 2011; Thomas and Davidson, 2012a, 2012b; and Frezzotti et al., 2012, HCO_3^- and CO_3^{2-} are common species dissolved in the aqueous phase of hydrothermal fluids, namely those that formed Sn-W deposits. However, we did not find these species in the analyzed fluid inclusions from the Carris ore deposit

8. Isotopic studies

In order to constrain the age of the mineralization and crust/mantle origin of the ore-forming fluids, rhenium-osmium and helium-argon isotope analysis of ore samples were carried out.

8.1. Molybdenite Re-Os data

The Re-Os data of molybdenite from the Carris quartz veins and surrounding Gerês granite indicate ages of 278.5 ±1.2 Ma and 280.3±1.2 Ma, respectively (Table 10). The age uncertainty is quoted at 2σ level, and includes all known analytical uncertainty, including a ~0.31% uncertainty in the decay constant of ^{187}Re. The Re content of the molybdenite is notably low, < 0.5 ppm.

8.2. Pyrite He-Ar data

The abundance of helium in the atmosphere is very low ($1.39x10^{-6}$ = 1 *Ra*), due to He escape to space, and the solubility of He in aqueous fluids is also low. Consequently it is unlikely that atmospheric-derived He affect the composition of crustal fluids in terms of He isotopes. Meteoric or marine air-saturated water (ASW) is characterized by Ar and He isotope compositions of $^{40}Ar/^{36}Ar$ =295.9 and $^{3}He/^{36}Ar$ =$5x10^{-8}$ similar to the atmospheric values, because ASW is in equilibrium with the atmosphere. The $^{40}Ar/^{36}Ar$ values range from 300±7 to 410 ±22. The $^{3}He/^{4}He$ is between 0.73 and 2.17 *Ra*. The $^{3}He/^{36}Ar$ values ($0.8\text{-}5x10^{-3}$) are much higher than those of air-saturated water, indicating that He in ore-forming fluids from Carris orebody is predominantly non-atmospheric in origin. The composition of ^{4}He ($9.43x10^{-7}$ to $3.70x10^{-6}$ cm^{-3} STP $^{4}He/g$) and ^{40}Ar ($3.91x10^{-7}$ to $1.37x10^{-6}$ cm^{-3} STP $^{40}Ar/g$) show variations that may reflect variable fluid inclusion abundance in the samples. Pyrite retains Ar and He for periods longer than 100 million years (Stuart et al., 1994). Cosmogenic incorporation of ^{3}He in the fluids can be ruled out because the samples were collected in the level 1 (old mining drawings, 1953). A contribution of ^{3}He from ^{6}Li decay is also unlikely due to the absence of Li-bearing minerals in the Carris ores. The in situ production of ^{40}Ar from fluid inclusions and mineral lattices are considered negligible considering the low diffusion of Ar in pyrite (York et al., 1982) and the extremely low concentration of K in pyrite (York et al., 1982). The amount of radiogenic ^{4}He produced from the decay of radioactive elements is within the analytical errors. Even though the trapped He and Ar are partially lost, the ratios $^{3}He/^{4}He$ and $^{40}Ar/^{36}Ar$ remain unchanged (Baptiste and Fouquet, 1996; Ballentine and Burnard, 2002; Hu et al., 2004). Fluids

responsible for Carris pyrite composition are derived from mantle and crust (Fig. 16). The noble gas compositions of volatiles released from Carris pyrite crystals are given in Table 11.

9. Discussion

9.1. Mineralogical data

Six generations of muscovite were found in the W-Mo-Sn quartz veins from Carris (Table 1 and Fig. 8) showing progressive higher Fe^{2+}, Mg, Li and F contents and lower Al^{VI} and OH contents (Table 3) from the first to the fourth generation, then they show opposite behaviours of those elements to the fifth generation, but return to the normal behaviours towards the sixth generation. Muscovite 5 surrounding wolframite and scheelite (Fig. 6c) has lower Fe^{2+} and F contents than muscovite 4 (Table 3) surrounding cassiterite (Fig. 6b), because wolframite and fluorite precipitated. Mg and Li contents also decrease from muscovite 4 to muscovite 5, because they were mainly retained in muscovite 4. Muscovites from Portuguese tin and tungsten deposits have a lower W content than Sn content. Both elements may be guides of Sn and W mineralizations (Neiva, 1987). The younger generation of rutile included in cassiterite has higher Nb, Ta, Sn and Fe contents and lower Ti content than the earlier generation of rutile included in muscovites of the first and second generations (Table 5). Two distinct generations of cassiterite occur (Table 1 and Fig. 8). The younger generation is the purer (Table 5), because it is one of the last minerals to crystallize as it occurs in veinlets cutting kesterite (Table 1), whereas the earlier generation occurs included in quartz and wolframite. The changes in compositions of muscovite and rutile are mainly attributed to a change in the mineralizing fluid composition, because muscovite 1 and rutile 1 belong to pegmatitic assemblages, whereas muscovites 2, 3 and 4 and rutile 2 belong to quartz vein assemblages (Fig. 8). Therefore, there was a change from magmatic fluids to magmatic hydrothermal fluids. The composition of cassiterite 1 from quartz veins is derived from magmatic hydrothermal fluids, whereas

cassiterite 2 in the sulphide assemblage (Fig. 8) had also some influence of meteoric fluids, recording tectonic activity.

The W-Mo-Sn quartz veins from Carris present two generations of wolframite (Table 1 and Fig. 8). The earlier generation contains 91 mol% hübnerite and the younger generation contains 26-57 mol% hübnerite. The change in wolframite composition results from the change in the fluid composition. The Nb_2O_5 content of wolframite from Carris shows a wide range (Table 5) and the richest wolframite in the Nb content also contains some Sn and Ta contents. The earlier wolframite is among the poorest in Nb^{5+}+ Fe^{3+}_{calc} (Fig. 10b), showing that the fluid was impoverished in Nb, because rutile retained some Nb content, but the earlier generation of cassiterite has very low Nb content (Table 5). However, afterwards during cooling the fluid became richer in Nb as the younger generation of wolframite retained a higher Nb content. There is no significant distinction in the Fe^{3+} content of the two generations of wolframite (Table 5) and consequently the significant variation in Nb content is not related to a local enrichment in Fe^{3+} as in Panasqueira (Neiva, 2008).

Scheelite partially replaces wolframite (Fig. 6f and Fig. 7b) and surrounds it. Scheelite precipitated at lower temperature and pressure and from an aqueous lower salinity fluid than wolframite according to the present study of fluid inclusions (Tables 8 and 9). Cooling of a solution of constant Ca/Fe ratio cannot cause the replacement of ferberite by scheelite (Table 5) as shown by Wood and Samson (2000). The Ca/Fe ratio of the ore-forming fluid increased from the precipitation of the earlier generation of wolframite to the precipitation of scheelite during cooling due to the decrease of Fe content, because wolframite precipitated, and the involvement of descending meteoric fluids. As usual, sulphides are the last ore minerals to precipitate when the fluid has the lowest temperature and pressure. Two generations of arsenopyrite and pyrite were distinguished (Table 1), but they have a similar composition in each sulphide (Table 6), because it may have been overshadowed by small variations of sulfur and oxygen activity of the hydrothermal fluid (Kerr et al., 1999).

A complex magmatic-hydrothermal continuum during the mineralizing process (e.g. Heinrich, 1990; 1995; Roberts et al., 1998) is suggested by timing and nature of the W-Mo-Sn quartz veins from Carris. These veins have a low Mo/W ratio, indicating that it was also low in the magmatic hydrothermal fluids and related to low oxygen fugacities in the ore magma system (Candela and Bouton, 1990), which is supported by the fact that the Carris granite contains more ilmenite than magnetite (Neiva, 1993) and consequently has a low oxygen fugacity. Cassiterite is also derived from the magmatic hydrothermal system. The Carris granite, that has a close age to that of the mineralized quartz veins, contains 12±8 ppm Sn (Neiva, 1993) and is not a Sn-bearing granite, as it has less than 18-26 ppm Sn (Lehmann, 1987), but fractional crystallization caused the Sn enrichment. The quartz veins studied here contain W>Mo>Sn, because enrichment of initial melts in W and Mo is not necessary and oxygen fugacity can significantly affect the W/Mo rating in a magmatic hydrothermal mineral deposit (Candela and Bouton, 1990).

9.2. Age of mineralization

The Re content of molybdenite from the Carris W-Mo-Sn quartz veins is very low < 0.5 ppm, indicating that Re is bonded in the molybdenite crystal structure, which is important from the geochronological point of view (Drábek et al., 2010). The Re-Os age of 279.4±1.2 Ma of this molybdenite (Table 10) is in excellent agreement with the ID-TIMS U-Pb zircon age of 280±5 Ma for the Carris granite, taken as a minimum emplacement granite age (Dias et al., 1998), suggesting that these veins are related to the Carris granite. The circulation of the mineralizing fluids could have taken place up to 1-4 Ma after the emplacement of the Carris granite. K-Ar data of muscovites from W-Mo quartz vein and host granite from Hwanggangri district, Korea are very similar (So, 1994). The Re-Os dating of molybdnenite shows that tin mineralization and the emplacement of the Sn-specialized granite from Erzgebirge fall in a narrow range up to 5 Ma (Romer et al., 2007). The Cu-Au-(W-Bi-Sn) deposit from Carajás, Brazil, gives an age indistinguishable from the ages of the host granites (Tellarico et al., 2004). Snee et al., (1988)

based on $^{40}Ar/^{39}Ar$ age concluded that at the Portuguese Panasqueira W-deposit the ore deposition occurred from 296 to 292 Ma. Therefore, the Panasqueira hydrothermal system is older than the Carris system. The age of 279.4±1.2 Ma for molybdenite from the W-Mo-Sn quartz veins of Carris agrees with ages obtained for hydrothermal vein deposits in other parts of Europe (Bielicki and Tischendorf, 1991; Pfaff et al, 2009) with a distinct maximum age of 270-280 Ma (Romer et al. 2010). The mineralized quartz veins from Carris present a post-D3 Variscan age, suggesting that this hydrothermal mineralization is related to changes in stress patterns during post-Variscan plate reorganization, as in Central Europe (Pfaff et al., 2009) causing the intrusion of the Carris granite, the most likely igneous source for the metal content of the orebody, due to its age determined by a precise method (ID-TIMS U-Pb of zircon, Dias et al., 1998).

Taking into account the age errors, the Re-Os age (279.4±1.2 Ma) of molybdenite from the Carris ore deposit (this study) is within the K-Ar age (273.6±11.7 Ma) of microcline from episyenites derived from the alteration of the Gerês granite (Jaques, 2008).

9.3. Origin of the mineralized fluids

Helium data represent a mixture of a magmatic mantle fluid component with a radiogenic He-rich crustal fluid (Fig. 16). The modification of the mantle signature probably resulted from two processes. (1) Dilution caused by the incorporation of radiogenic He-derived from melting of the crust; (2) Radiogenic helium assimilated from meteoric waters that circulate in the upper crustal levels, and also probably some fluids released from metasediments and host granites, have been incorporated in the hydrothermal fluids. The high $^{3}He/^{36}Ar$ ratio of Carris fluids (Table 11) indicates a mantle contribution. Mendes and Dias (2004) proposed that the entire Peneda-Gerês pluton was a product of mantle input followed by mantle-crust interaction. At Carris the $^{3}He/^{4}He$ (*Ra*) ratio ranges between 0.73 and 2.17. Other W deposits have similar *Ra* ratios, indicative of a mantle contribution for the mineralized fluids, namely the World-class Chinese deposits of Shizhuyuan (*Ra* 0.06-1.66, Stuart et al., 1994), Yaogangxian (*Ra* 0.41-3.03,

Zhao et al., 2002) and Sn-gigantic deposit of Dachang (*Ra* 1.7-2.5, Wu et al., 2011) and the Korean Dae-Hwa W-Mo deposit (*Ra* 0.15-1.4, Hu et al., 2012). One of the highest mantle contributions in mineralizing fluids ever registered occurs in the Portuguese Panasqueira W-mine with *Ra* ~5, around 75% of mantle input (Burnard and Polya, 2004). The fact that this mantle signature was found in pyrite and that this mineral precipitated in the sulphide stage after the deposition of wolframite and scheelite indicates that the magmatic fluid was part of the mineralizing fluid during the major part of the hydrothermal event. The scheelite has probably resulted from the mixture of Ca-rich meteoric water with the W-rich hydrothermal-magmatic fluid. The origin of calcium lies most probably in the argilization of feldspar present in the former granitic and/or metasedimentary country rocks already eroded. Taking into account the average content of CaO in the Gerês and Carris granites (1.19% CaO-Neiva, 1993) towards the formation of the whole scheelite deposit would be required leach less than 1 % of the calcium content in a section of the enclosing rock of 10 x 1000 x 7000 m.

9.4. P-T-X-depth characteristics of the mineralized fluids

In order to estimate the P-T depth for the ore deposition conditions, a series of isochores representative of the observed fluids were drawn (Fig. 17). The absence of evidence of boiling and heterogeneous fluid trapping suggests that each of the fluid types was entrapped in one phase stability field. The CO_2 and N_2 content of the fluids could have resulted from the magmatic-hydrothermal fluids or derived from devolatilization of country rock organic matter-rich metasediments. The relatively wide salinity content for the aqueous carbonic fluid could have resulted from differential assimilation of Na^+ during the multiple percolation pathways of the channelized fluid trough the country rock. The homogenization temperatures for the aqueous carbonic fluids in the quartz associated with wolframite deposition define a lower limit for the corresponding pressure at homogenization and consequently for the pressure during the crystallization of quartz plus wolframite. Considering the isochore for the higher pressure-temperature conditions attending to these aqueous carbonic fluids, we can determine a value of

195 MPa for Th = 280ºC (mode value), which implies a depth of around 7 km considering a lithostatic pressure regime and rock density of 2.7 gcm^{-3}. At this depth the majority of the isochores occurs between 435 and 400ºC therefore we presume that the wolframite precipitation occurred mainly at this temperature range (Fig. 17). Since the aqueous carbonic fluids exhibit liquid and vapor CO_2 homogenizations, there must have been pressure fluctuations during their entrapment in an oscillatory regime probably linked to a seismic pumping fluid transport mechanism as in various analogous situations previously documented (Sibson, 1973, 1983, 1987, 1990; Sibson et al., 1975; Cathelineau et al., 1993; Vrolijk and Myers, 1990; Wilkinson and Johnston, 1996; Montomoli et al., 2001). This is very likely taking into account the regional extensional setting and the brittle tectonics that occurred after the collision between the Laurasia and Gondwana supercontinents at that time and paleogeographic location, which promoted seismic events and rapid fluid escape. The temperature of 280ºC is precisely the same at which the scheelite fluid inclusions exhibit the highest Th values (Fig. 17). According to the isochoric path for the scheelite fluids, the pressure at this temperature is ~70 MPa, which corresponds to a depth of 7 km for a fluid regime under hydrostatic conditions. This is the most probable if between the two tungstate depositions there was not significant erosion. Assuming a pressure regime between hydrostatic and lithostatic the entrapment could have occurred at higher pressure at the same depth. This depth is however a minimum depth at which the W deposition occurred at Carris. Although the upper limit for the depth of entrapment could not be constrained with precision, probably it was not much higher. The study carried out by Amossé (1976) in Borralha tungsten mine concluded that wolframite crystallized around 150 MPa. On the other hand, Noronha (1984b) proposed that wolframite precipitated around 65-100 MPa under lithostatic conditions, what implies a depth between 2.5 and 3.7 km. Noronha and Ribeiro (1983) suggested that the contact metamorphism generated by the Gerês granite attained 200 MPa, a value that could be considered an upper limit for the pressure in this zone. The hydrothermal fluid temperature probably lay between 340-270 ºC when scheelite deposited at Carris. In general there are three main reasons for scheelite deposition: a temperature fall

between 450 and 300ºC, pH changes and local calcium enrichment in the hydrothermal solutions due to interaction with the country rocks (Rafal'skiy et al., 1984). The fact that the Carris scheelite precipitated after wolframite, from aqueous low salinity fluids, is according with an hypothesis of a drastic change in the pressure regime from lithostatic to hydrostatic, which promoted the assimilation (mixture) of meteoric waters by the hydrothermal fluid with a magmatic affinity. We have not found evidence to constrain the P-T conditions at deposition for cassiterite and molybdenite (the other economic minerals in this deposit), but according to their position on the paragenesis it is likely that the first generation of cassiterite precipitated at similar wolframite conditions. Like scheelite, molybdenite probably deposited at an hydrostatic pressure regime. The other minerals namely the third generation of beryl and fluorite precipitated after scheelite during the lowering of the temperature of the hydrothermal system. This type of fluid displays similar features to those found as secondary fluid inclusions trails within quartz and probably represents the last imprint of the hydrothermal circulation in this deposit. According to Wood and Samson (2000) the W hydrothermal fluids on ore quartz veins are either aqueous or aqueous carbonic fluids with salinities normally ranging from 0-15 wt. %. The CO_2 is common and could achieve 45% of the bulk fluid. Other frequent gases are CH_4 and N_2. The same authors concluded that most W minerals deposited in the range 200 to 500ºC and between 20 to 150 MPa, with a decrease in temperature through the paragenesis. The sulphide stage, that is a normal characteristic in these deposits, normally postdated the W stage, but in some deposits the stages are overlapped. At Carris the fluids responsible for wolframite deposition are H_2O-CO_2-N_2-NaCl with salinities ranging from 0.04-5.25 mol% (0.1-17 % wt. eq. NaCl) and with Th between 276ºC-310ºC (mode around 290ºC). These Th are minimum possible temperatures for the deposition; the probable entrapment temperatures are thus ≥ 310ºC.

The main mechanisms considered for the beginning of wolframite precipitation are boiling (e.g. Graupner et al., 1999), fluid mixing (e.g. Wei et al., 2012), boiling and mixing processes (e.g. Wei et al., 2012), cooling (e.g. Xi et al., 2008), pressure decrease (Polya, 1989) and wall-

reactions (Gong et al., 2004). Most of the PTX characteristics for the Carris fluids are identical to others from many W-deposits, although some studies refer the involvement of a $NaHCO_3$ component in the fluid phase (e.g. Thomas et al., 2011). The Panasqueira underground W(-Sn-Cu) active mine is a World Class deposit working since 1896. The deposit was extensively studied over the last decades (e.g. Thadeu, (1951, 1979), Kelly and Rye (1979), Bussink (1984), Noronha et al. (1992), Foxford et al. (2000), Polya et al. (2000), Burnard & Polya (2004)). It is composed of a set of subhorizontal hydrothermal quartz veins with wolframite as the dominant ore mineral, hosted in Cambrian and Precambrian schists and greywackes. In the lower levels of the mine a greisenised granitic cupola is exposed. At Panasqueira, wolframite deposition was achieved at a temperature between 230-360 ºC from H_2O-CO_2-CH_4-N_2-NaCl hydrothermal fluids (Kelly, 1977). The gases are thought to be derived from organic-matter rich-metasediments desvolatilisation. Salinities are mostly between 5 and 10 NaCl wt.%. At Panasqueira there are evidences of strong pressure fluctuations during the precipitation of the main oxide stage (Lourenço, 2002) although in general the fluids lose their gas content during the evolution of the hydrothermal event. Except for the fact that at Panasqueira the aqueous carbonic fluids have CH_4 (although generally as low as 0.1-0.2 mol%) the physical chemical characteristics of the ore-forming fluids are very similar to the Carris hydrothermal fluids. The Borralha mine is composed of a series of vertical and subhorizontal quartz veins and two mineralized collapse breccias. According to Noronha (1984a,b) the paragenesis is composed of three wolframite generations and one primary scheelite deposition (with no cassiterite); the W minerals formed during two main episodes, decreasing slightly from 330 to 290ºC through a decreasing salinity (from 10 to 2 eq.wt % NaCl) with acid fluids dominated by Na^+, Cl^- and admittedly also HCO_3^-. The wolframite crystallized at 65-100 MPa, a pressure lower than in the Carris deposit. The W deposition at Massif Central (France) and Cornwall (Great Britain) Variscan mining districts occurred from homogeneous H_2O-CO_2-CH_4-NaCl fluids at 400-450ºC and ~100 MPa probably as a consequence of isobaric cooling (Charoy, 1979; Ramboz, 1980; Dubessy et al., 1987). These PTX conditions are similar to those observed at the Carris deposit.

A recent study on the metallogeny of the giant Chinese quartz vein Xihaushan W-deposit (Wei et al., 2012) revealed that wolframite precipitated due to mixing of a tungsten-bearing magmatic fluid and a meteoric fluid, following a decrease of temperature (from 380ºC to 236ºC) and lowering of chloride concentration. Also the deposition of the main mineralization from the Korean Dae Hwa W-Mo vein deposit occurred from a decreasing temperature (400 to 230ºC) as a result of mixing of a magmatic hydrothermal fluid with meteoric cooler waters (Stuart et al., 1994), a mechanism that seems to have occurred at Carris during scheelite deposition. Recently, Ortelli and Kouzmanov (2011) concluded that wolframite from Morococha, a Cordilleran polymetallic vein deposit in Peru, crystallized around 300 ºC from low salinity fluids (1-1.3 eq. wt % NaCl). Both salinity and temperature of wolframite deposition lie within the range observed for the Carris orebody. The fluid inclusions studies in quartz from episyenites (Jaques et al., 2010) and in scheelite from the W-Mo-Sn quartz veins from Carris (this study) show low salinity aqueous fluids without detectable CO_2. Those from episyenites have lower temperatures and mean salinity value than those of scheelite from the mineralized quartz veins of Carris (Fig. 17), suggesting that episyenites are later than quartz veins. However, field evidence, mineralogical studies and geochemistry of rocks suggest that immediately after the opening of fractures for the hydrothermal system, K-feldspar from host granite becomes reddish and its triclinicity increased. An hematite powder is disseminated in the K-feldspar and Fe^{3+} replaces Al. Biotite starts to alter into chlorite, plagioclase is altered loosing some anorthite content and albite and secondary muscovite and pistacite are formed. Albite, chlorite I, pistacite and hematite occur early in the mineralized quartz veins (Fig. 8) and increase significantly in episyenites which end to be formed after the W-Mo-Sn quartz veins due to the intense circulation of the low salinity aqueous fluids, which cause the highest degree of hydrothermal alteration of granite.

9.5 Origin, transport and deposition of tungsten of the Carris ore deposit

The Carris ore deposit is associated with granites (Fig. 3). The tungsten is probably derived from a fluid that has equilibrated with the Carris granite and related granitic pegmatites, as the

mineralized quartz veins and this granite are of the same age. Tungsten is not concentrated in minerals from granite and granitic pegmatites due to its radius and charge. It will be concentrated in the residual magma and magmatic hydrothermal fluids due to fractional crystallization. The magmatic hydrothermal fluids are very rich in SiO_2. Tungsten was probably transported as tungstate species H_2WO_4, HWO_4^-, WO_4^{2-}, and alkali-tungstate ion pairs (Wood and Samson, 2000). Tungsten precipitated as wolframite probably due to pressure fluctuations in a gradual temperature and pressure decrease of the hydrothermal system. However, scheelite would have precipitated due to mixing processes of hotter and colder fluids.

Acknowledgements

The authors thank the Portuguese Foundation of Science and Technology (FCT) for the financial support; Rui Zhong Hu (State Key Laboratory of Ore Deposits Geochemistry, Institute of Geochemistry, Chinese Academy of Sciences, Guiyang, China) for providing the isotope analysis of helium and argon obtained at his laboratory; Fernando Noronha, coordinator of CGUP, for permitting to use some samples from the Carris mine and Fernanda Guimarães (LNEG) for having helped to obtain analysis with the electron microprobe. We thank Rainer Thomas and an anonymous referee for their helpful comments. We also thank Reimar Seltmann for the editorial work.

References

Amossé J. Détermination expérimentale de la température de formation d'un filon quartzeux wolframifère. Approche théorique. Bulletin de la Société française de minéralogie et de cristallographie 1976;99:121-127.

Bakker RJ. Adaptation of the Bowers and Helgeson (1983) equation of state to the H_2O–CO_2–CH_4–N_2–NaCl system. Chemical Geology 1999;154:225-236.

Bakker RJ. Package FLUIDS 1. Computer programs for analysis of fluid inclusion data and for modeling bulk fluid properties. Chemical Geology 2003;194:3-23.

Ballentine CJ, Burnard PG. Production, release and transport of noble gases in the continental crust. Reviews in Mineralogy and Geochemistry 2002;47:481-538.

Baptiste PJ, Fouquet Y. Abundance and isotopic composition of helium in hydrothermal sulfides from the East Pacific Rise at 13 N. Geochimica et Cosmochimica Acta 1996; 60:87-93.

Bente K, Doering T. Solid-state diffusion in sphalerite: an experimental verification of the chalcopyrite disease. European Journal of Mineralogy 1993;5:465-478.

Bielicki KH, Tischendorf G. Lead isotope and Pb-Pb model age determinations of ores from Central Europe and their metallogenetic interpretation. Contributions to Mineralogy and Petrology 1991;106:440-461.

Bodnar RJ. Revised equation and table for determining the freezing point depression of H_2O-NaCl solutions. Geochimica et Cosmochimica Acta 1993;57:683-684.

Bowers TS, Helgeson HC. Calculation of the thermodynamic and geochemical consequences of nonideal mixing in the system H_2O–CO_2–NaCl on phase relations in geological systems: equation of state for H_2O–CO_2–NaCl fluids at high pressures and temperatures. Geochimica Cosmochimica Acta 1983;47:1247–1275.

Burnard PG, Polya DA. Importance of mantle derived fluids during granite associated hydrothermal circulation: He and Ar isotopes of ore minerals from Panasqueira. Geochimica Cosmochimica Acta 2004;68 (7):1607-1615.

Bussink RW. Geochemistry of the Panasqueira tungsten-tin deposit, Portugal. Geologica Ultraiectina 1984;33, 170 pp. Ph.D.thesis Holland.

Candela PA, Bouton SL. The influence of oxygen fugacity on tungsten and molybdenum partitioning between silicate melts and ilmenite. Economic Geology 1990;85:633-640.

Cathelineau M, Boiron MC, Essarraj S, Dubessy J, Lespinasse M, Poty B. Fluid pressure variation in relation to multistage deformation and uplift: a fluid inclusion study of Au quartz veins. European Journal of Mineralogy 1993; 5:107-121.

Charoy, B. Greisenisation, minéralisation et fluides associés à Cligga Head, Cornwall. Bulletin de Minéralogie 1979;102:633-641.

Cheilletz A, Giuliani G. The role of deformation and the geneses of the feldspathic episyenitic rocks from Lovios - Gerês Mountains (Galice) and Zaer (Central Morocco). Mineralium Deposita 1982;17,3: 387-400.

Cook NJ, Chryssoulis SL. Concentrations of "invisible gold" in the common sulfides. Canadian Mineralogist 1990;28:1-16.

Cottard F. Petrologie structural et métallogénie du complexe granitique de Lovios Geres. Le modele de mise en place de la mine de Las Sombras (Sn-W-Mo-Bi) (Sud-Galice, Espagne). These de 3 ème cycle, 1979. Universite de Nancy, France.

Dias G, Leterrier J, Mendes A, Simões PP, Bertrand JM. U-Pb zircon and monazite geochronology of post-collisional Hercynian granitoids from Central Iberian Zone (Northern Portugal). Lithos 1998;45:349-369.

Dias R, Ribeiro A. The Ibero-Armoriean Are: a collision effect against an irregular continent? Tectonophysics 1995,246: 113-128.

Drábek M, Rieder M, Böhmová V. The Re-Mo-S system: new data on phase relations between 400 and 1200ºC. European Journal of Mineralogy 2010;22:479-484.

Dubessy J, Ramboz C, Nguyen TC, Cathelineau M, Charoy B, Cuney M, Leroy J, Poty B, Weisbrod A. Physical and chemical control (fO2–T–pH) of the opposite behaviour of U and Sn–W as exemplified by hydrothermal deposits in France and Great Britain, and solubility data.Bulletin Minéralogie 1987;110:261-281.

Ferreira N, Iglesias M, Noronha F, Pereira E, Ribeiro A, Ribeiro ML. Granitos da Zona Centro Iberica e seu enquadramento geodinamico. In: Bea, F., Carnicero, A., Gonzalo, J., Lopez Plaza, M., Rodriguez Alonso, M. (Eds.), GeologIa de los Granitoides y Rocas Asociadas deI Macizo Hesperico. Editorial Rueda, Madrid, pp. 37-51. Libro de Homenaje a L.C. Garcia de Figuerola 1987.

Foxford KA, Nicholson R, Polya DA, Hebblethwaite RPB. Extensional failure and hydraulic valving at Minas da Panasqueira, Portugal: evidence from vein spatial distributions, displacements and geometries. Journal of Structural Geology 2000;22:1065-1086.

Frezzotti ML, Tecce F, Casagli, A. Raman spectroscopy for fluid inclusion analysis. Journal of Geochemical Exploration 2012;112:1-20.

Gong GJ, Yu CW, Zhang RH. Physical chemistry study on the ore-forming process of Shizhuyuan tungsten-polymetallic deposit (in Chinese with English abstract). Earth Science Frontiers 2004;11:617-625.

Graupner T, Kempe U, Dombon E, Pätzold O, Leeder O, Spooner ETC. Fluid regime and ore formation in the tungsten (-yttrium) deposits of Kyzyltan (Mongolia Altai): evidence for fluid variability in tungsten-tin ore systems. Chemical Geology 1999;154:21-58.

Heinrich CA. The chemistry of tin (-tungsten) ore deposition. Economic Geology 1990;85:529-550.

Heinrich CA. Geochemical evolution and hydrothermal mineral deposition in Sn (-W-base metal) and other granite related ore systems, some conclusions from Australian examples. In: Thompson JFH. Editor. Magmas, fluids and ore deposits: Mineral Association of Canada Short Course Series 1995;23:203-220.

Hu RZ, Burnard PG, Bi XW, Zhou MF, Peng JT, Su WC, Wu KX. Helium and argon isotope geochemistry of alkaline intrusion-associated gold and copper deposits along the Red River-Jingshajiang fault belt, SW China. Chemical Geology 2004;203:305-317.

Hu RZ, Bi XW, Jiang GH, Chen HW, Peng JT, Qi YQ, Wu LY, Wei WF Mantle-derived noble gases in ore-forming fluids of the granite-related Yaogangxian tungsten deposit, Southeastern China, Mineralium Deposita 2012;47:623-632.

Kelly WC. The relative timing of metamorphism, granite emplacement and hydrothermal ore deposition in the Panasqueira district (Beira Baixa, Portugal). Comunicações dos Serviços Geológicos de Portugal 1977;61:239-244.

Kelly WC, Rye RO. Geologic, fluid inclusions and stable isotope studies of the tin-tungsten deposits of Panasqueira, Portugal. Economic Geology 1979;74:1721-1822.

Kerr LC, Craw D, Youngon JH. Arsenopyrite compositional variation over variable temperatures of mineralization, Otago schist, New Zealand. Economic Geology 1999;94:123-128.

Knight CL, Bodnar RJ. Synthetic fluid inclusions: IX. Critical PVTX properties of NaCl-H_2O solutions. Geochimica Cosmochima Acta 1989;53:3-8.

Jackson NJ, Willis-Richards J, Maning DAC, Sams M. Evolution of the Cornubian Ore Field, southwest England: part II. Mineral deposits and ore-forming processes. Economic Geology 1989;84:1101-33.

Jaques L. Estudo da episssienitização de granitos da "Zona Centro-Ibérica". Contribuição para a caracterização dos processos hidrotermais pós-magmáticos. Ph D thesis. Universidade do Porto 2008;506 pp.

Jaques L., Bobos I., Noronha F. Study of fluids related to hydrothermal alteration of biotite granites from Geres and Guarda (Portugal). Comunicações Geológicas 2010;97:81-98.

Julívert M., Fontboté J.M., Ribeiro A, Conde L. Mapa tectónico de la Península Ibérica y Baleares, escala 1:1 000000, 113p. Instituto. Geologico y Mineiro. Espana 1974.

Lehmann B. Tin granites, geochemical heritage, magmatic differentiation. Geologische Rundschau 1987;76:177-185.

Lourenço A. Paleofluidos e mineralizações associadas às fases tardias da Orogenia Hercínica 2002. 326 pp. Ph.D.thesis University of Porto, Portugal.

Marignac C., Cuney M. Ore deposits of the French Massif Central: insight into the metallogenesis of the Variscan collision belt. Mineralium Deposita 1999;34:472-504.

Markey RJ, Stein HJ, Morgan JW. Highly precise Re-Os dating for molybdenite using alkaline fusion and NTIMS. Talanta 1998;45:935–946.

Markey R, Stein HJ, Hannah JL, Zimmerman A, Selby D, Creaser RA. Standardizing Re-Os geochronology: A new molybdenite Reference Material (Henderson, USA) and the stoichiometry of Os salts". Chemical Geology 2007;244:74-87.

Mattauer M, Etchecopar A. Arguments en faveur de chevauchements de type himalayen dans la chaine hercynienne du Massif Central Français. In: Coll Int C.N.R.S, Ecologie et Geologie de l'Himalaya, Paris, 1976, C.N.R.S. 1977;268:261-267.

Mendes ACM. Geocronologia e petrogénese do maciço granítico pós-tectónico de Peneda-Gerês (ZCI, norte de Portugal e Galiza). Unpublished PhD thesis, University of Minho 2001. 275 pp.

Mendes AC, Dias G. Mantle-líke Sr-Nd isotope composition of Fe-K subalkalíne granites: the Peneda-Geres Variscan massif (NW Iberian Peninsula). Terra Nova 2004;16:109-115.

Mills RA, Fine HD. Report to Sociedade das Minas do Gerez, Lda. 1972.

Montomoli C, Ruggieri G, Boiron MC, Cathelineau M. Pressure fluctuation during uplift of the Northern Apennines (Italy): a fluid inclusion study. Tectonophysics 2001;341:121-139.

Moura A. Metais e semi-metais de Portugal. Coimbra (Portugal): Palimage; 2010.

Neiva AMR. Geochemistry of white micas from Portuguese tin and tungsten deposits. Chemical Geology 1987;63:299-317.

Neiva AMR. Geochemistry of granites and their minerals from Gerez mountain, northern Portugal. Chemie der Erde 1993;53:227-258.

Neiva AMR. Gold-quartz veins at Gralheira, northern Portugal: mineralogical and geochemical characteristics. Transactions of the Institution of Mining and Metallurgy (Section B: Applied Earth Science) 1994;103B:188-196.

Neiva AMR. Geochemistry of cassiterite and its inclusions and exsolution products from tin and tungsten deposits in Portugal. Canadian Mineralogist 1996;34:745-768.

Neiva AMR. Portuguese granites associated with Sn-W and Au mineralizations. Bulletin Geological Society of Finland 2002;74 (1-27):79-101.

Neiva AMR. Geochemistry of cassiterite and wolframite from tin and tungsten quartz veins. Ore Geology Reviews 2008;33:221-238.

Neiva AMR, András P, Ramos, JMF. Antimony quartz and antimony-gold quartz veins from northern Portugal. Ore Geology Reviews 2008;34:533-546.

Neiva AMR, Ramos JMF. Geochemistry of granitic aplite-pegmatite sills and petrogenetic links with granites, Guarda-Belmonte area, central Portugal. European Journal of Mineralogy 2010;22:837-854.

Noronha F. Mineralizações espacial e geneticamente associadas ao maciço granítico da Serra do Gerês. Um exemplo de zonalidade. Cuadernos do Laboratorio Xeolóxico de Laxe 1984a;7:87-99.

Noronha F. Caractéristiques physico-chimiques des fluides associes à la génese du gisement de tungstène de Borralha (North Portugal). Bulletin Minéralogie 1984b;107:273-284.

Noronha F, Dória A, Dubessy J, Charoy B. Characterization and timing of the different types of fluids present in the barren and ore-veins of the W-Sn deposit of Panasqueira, Central Portugal. Mineralium Deposita 1992;27:72-79.

Noronha F, Ribeiro ML. Mapa e Notícia Explicativa da folha 6-A da Carta Geológica de Portugal à escala 1:50 000. Serviços Geológicos de Portugal 1983, Lisboa.

Ortelli M, Kouzmanov K. Fluid inclusion microthermometry in coexisting quartz and wolframite- a case study from Morococha, Peru. In: Bakker RJ, Baumgartner M, Doppler G editors. European Current Research on Fluid Inclusions (ECROFI-XXI) Abstracts. Berichte der Geologischen Bundesanstalt 2011;87:154-155.

Pfaff K, Romer RL, Markl G. U-Pb ages of ferberite, chalcedony, agate, U-mica and pitchblende: constraints on the mineralization history of the Schwarzwald ore district. European Journal of Mineralogy 2009;21:817-836.

Polya DA. Chemistry of the main-stage ore-forming fluids of the Panasqueira W-Cu (Ag)-Sn deposit, Portugal: implications for models of ore genesis. Economic Geology 1989;84:1134-1152.

Polya DA, Foxford KA, Stuart F, Boyce A, Fallick AE. Evolution and paragenetic context of low δD hydrothermal fluids from the Panasqueira W-Sn deposit, Portugal: New evidence from microthermometric, stable isotope, noble gas and halogen analyses of primary fluid inclusions. Geochimica et Cosmochimica Acta 2000;64(19):3357-3371.

Poty B, Leroy J, Jachimowicz L. Un novel appareil pour la mesure des températures sous le microscope: L'installation de microthermométrie Chaixmeca. Bulletin de Minéralogie 1976;99:182-186.

Prieto AC, Guedes A, Dória A, Noronha F, Jiménez J. Quantitative determination of gaseous phase compositions in fluid inclusions by Raman microspectrometry. Spectroscopy Letters 2012;45:156-160.

Rafal'skiy RP, Bryzgalin OV, Fedorov PL. Tungsten migration and scheelite deposition under hydrothermal conditions. Geochemistry International 1984;21:1-13.

Ramboz C. Géochimie et Etude des Phases Fluides de Gisements et indices d'etain-tungstene du Sud du Massif Central (France). 1980 278 pp. PhD thesis INPL Nancy, France.

Roberts S, Sanderson DJ, Gumiel P. Fractal analysis of Sn-W mineralization from Central Iberia: Insights into the role of fracture connectivity in the formation of an ore deposit. Economic Geology 1998;93:360-365.

Roedder E. Fluid Inclusions. Reviews in Mineralogy volume 12; Mineralogical Society of America. Paul H. Ribbe (Series Editor). 1984.

Romer RL, Thomas R, Stein HJ, Rhede D. Dating multiply overprinted Sn-mineralized granites – examples from the Erzgebirge, Germany. Mineralium Deposita 2007;42:337-359.

Romer RL, Schneider J, Linnemann U. Hydrothermal vein mineralization-markers for post-Variscan brittle deformation of Western Europe: a geochronologic review. In: Linnemann U, Romer RL, editors. Pre-Mesozoic Geology of Saxo-Thuringia. From the Cadomian Active Margin to the Variscan Orogen: the pre-Mesozoic geology of Saxo-Thuringia (NE Bohemian Massif). Schweizerbart Science Publishers, Stuttgart; 2010. p. 347-360.

Selby D, Creaser RA. Macroscale NTIMS and microscale LA-MC-ICP-MS Re-Os isotopic analysis of molybdenite: Testing spatial restrictions for reliable Re-Os age determinations, and implications for the decoupling of Re and Os within molybdenite. Geochimica et Cosmochimica Acta 2004;68:3897-3908.

Shepherd T. Temperature-programmable heating-freezing stage for microthermometric analysis of fluid inclusions. Economic Geology 1981;76:1244-1247.

Sibson R. Interactions between temperature and pore-fluid pressure during earthquake faulting and a mechanism for partial or total stress relief. Nature 1973;243:66-68.

Sibson R. Continental fault structure and the shallow earthquake source. Journal of Geological Society of London 1983;140:741-767.

Sibson R. Earthquake rupturing as a mineralizing agent in hidrothermal systems. Geology 1987;15:701-704.

Sibson R. Faulting and fluid flow. Fluids in tectonically active regimes of the continental crust. In: Nesbitt BE editor. Mineralogical Association of Canada, Short Course Handbook, Vancouver, B.C. 1990; 18: 93-132.

Sibson R, Moore McM, Rankin A. Seismic pumping- a hidrothermal fluid transport mechanism. Journal of Geological Society of London 1975;131:653-659.

Snee LW, Sutter JF, Kelly WC. Thermochronology of economic mineral deposits: dating the stages of mineralization at Panasqueira, Portugal, by high-precision 40Ar/39Ar age spectrum techniques on muscovite. Economic Geology 1988;83:335-354.

So C-P. Origin and evolution of W-WO-producing fluids in a granitic hydrothermal system: geochemical studies of quartz vein deposits around the Susan granite, Hwanggangri district, Republic of Korea. Economic Geology 1994;89:246-267.

Štemprok M. Tin and tungsten deposits of the West Central European Variscides. Proceedings Fifth IACGOD Symposium. Utha1981, p. 495-512.

Štemprok M, Seltmann R. The metallogeny of the Erzgebirge (Krušné Hory). In: Metallogeny of Collisional Orogens (eds. Seltmann, Kampf, Mollers) 1994;61-69. Czech Geol. Survey, Prag.

Stuart FM, Turner G, Taylor R. He-Ar isotope systematics of fluid inclusions:resolving mantle and crustal contributions to hydrothermal fluids. In: Matsuda J editor. Noble Gas Geochemistry and Cosmochemistry. Tokyo: Terra Scientific Publishing Company (TERRAPUB); 1994. p. 261-277.

Sun, Q, Qin, C. Raman OH stretching band of water as an internal standard to determine carbonate concentrations. Chemical Geology 2011;282:274-278.

Thadeu D. Geologia do Couto Mineiro da Panasqueira. Comunicações Serviços Geológicos Portugal 1951;32:5-64.

Thadeu D. Le gisement stanno-wolframifère de Panasqueira (Portugal). Chronique de la Recherche Minière 1979;450:35-42.

Thomas R, Davidson P. The application of Raman spectroscopy in the study of fluid and melt inclusions. Zeitschrift der Deutschen Gesellschaft für Geowissenschaften 2012a;163:113-126.

Thomas R, Davidson P. Water in granite and pegmatite-forming melts. Ore Geology Reviews 2012b;46:32-46.

Thomas R, Davidson P, Schmidt C. Extreme alkali bicarbonate- and carbonate- rich fluid inclusions in granite pegmatite from the Precambrian Rønne granite, Bornholm Island, Denmark. Contribution to Mineralogy and Petrology 2011;161:315-329.

Thomas R, Davidson P, Beurlen H. The competing models for the origin and internal evolution of granitic pegmatites in the light of melt and fluid inclusion research. Mineralogy and Petrology 2012;106:55-73.

Tellarico FHB, McNaughton NJ, Groves DI, Fletcher IR, Figueiredo BR, Carvalho JB, Rego JL, Nunes AR, Geological and SHRIMP II U-Pb constraints on the age and origin of the Breves Cu-Au-(W-Bi-Sn) deposit, Carajás, Brazil. Mineralium Deposita 2004;39:68-86.

Tischendorf G, Gottesmann B, Förster H-J, Trumbull RB. On Li-bearing micas: estimating Li from electron microprobe analyses and an improved diagram for graphical representation. Mineralogical Magazine 1997;61:809-834.

Vindel E, Lopez JA., Boiron MC, Cathelineau M, Prieto AC. P-V-T-X-fO2 evolution from wolframite to sulphide depositional stages in intragranitic W-veins. An example from the Spanish Central System. European Journal of Mineralogy 1995;7:675-688.

Vrolijk P, Myers G, Fluid pressure history in subduction zones: evidence from fluid inclusions in the Kodiak Accretionary Complex, Alaska. In: Studies in Geophysics: The role of fluids in crustal processes, 1990; 148-157. National Academy Press, Washington, D.C.

Weeks JP. The Carris Wolfram Mine, Portugal. Report. 1979.

Wei W, Hu R, Bi X, Peng J, Su W, Song S, Shi S. Infrared microthermometric and stable isotopic study of fluid inclusions in wolframite at the Xihuashan tungsten deposit, Jiangxi province, China. Mineralium Deposita 2012;47:589-605.

Wilkinson J, Johnston J. Pressure fluctuations, phase separation, and gold precipitation during seismic fracture propagation. Geology 1996;24, 5: 395-398.

Wood SA, Samson I. The hydrothermal geochemistry of tungsten in granitoid environments. I. Relative solubilities of ferberite and scheelite as a function of T, P, pH and m_{NaCl}. Economic Geology 2000;95:143-182.

Wu LY, Hu RZ, Peng JT, Bi XW, Jiang GH, Chen HW, Wang QY, Liu YY. He and Ar isotopic compositions and genetic implications for the giant Shizhuyuan W-Sn-Bi-Mo deposit, Hunan Province, South China. International Geology Review 2011;53:677-690.

Xi BB, Zhang DH, Zhon LM, Zhang WH, Wang C. Characteristics of ore-forming fluid evolution in Dijishan tungsten deposit, Quannan county, Jiangxi (in Chinese with English abstract). Acta Geologica Sinica 2008;82:956-966.

York D, Masliwec A, Kuybida P, Hanes JE, Hall CM, Kenyon WJ, Spooner ETC, Scott SD. $^{40}Ar/^{39}$ Ar dating of pyrite. Nature 1982;300:52-53.

Zhao K, Jiang S, Xiao H, Ni P. Origin of ore-forming fluids of Dachang Sn-polymetallic ore deposit; evidence from helium isotopes. Chinese Science Bulletin 2002;47:1041-1045.

CAPTION

Fig. 1- European Variscides W-Sn ore province. Adapted from Štemprok, 1981.

Fig. 2A- Portuguese tungsten occurrences (most was exploited during World War II). CIZ- Central Iberian Zone, OMZ- Ossa Morena Zone, SPZ- South Portuguese Zone. Adapted from National Laboratory of Energy and Geology (LNEG) data.

Fig. 2B- Location and regional setting of the Carris W-Mo-Sn vein deposit, northern Portugal. 1- Silurian metasediments; 2- syn-D3 migmatite-granite complex; 3- syn-D3 two-mica granite; 4- late-D3 biotite granite; 5- post-D3 Gerês granite; 6- post-D3 Carris granite; 7- Gerês fault; 8- Portugal-Spain border. Adapted from Noronha and Ribeiro, 1983.

Fig. 3- Geological map at the Carris – Las Sombras area. Adapted from Cottard,1979. Yellow- Gerês granite; Red- Carris granite; 1- Quartz vein system; 2- Episyenite; 3- Fault; 4- Portuguese-Spanish border; 5- Geodesic mark.

Fig. 4- Structural analysis of the clusters of mineralized veins and its surround hydrothermal alteration focused by post-Variscan multistage shear. At the early episodes pegmatite assemblages may alternate with hydrothermal quartz-oxide-sulphide paragenesis.

Fig. 5- Porosity filling and stretched arrangement of some vein minerals and vein-related alteration products at the host granite after syntaxial pegmatite to quartz fractionation during shear and dilation – beryl may crystallize in shear related porosity after microcline generation and before quartz filling.

Fig. 6- Backscattered electron images of minerals of W>Mo>Sn quartz veins from Carris, northern Portugal. (a) Unzoned fluorite (Fl) and early oscillatory zoned muscovite (Mu) included in albite (Ab). (b) Cassiterite (Cst) included in zoned muscovite and quartz (Q). (c)

Late oscillatory zoned muscovite with an inclusion of scheelite (Sch), partially surrounding wolframite (W) and included in quartz. (d) Zoned chlorite (Chl) included in quartz. (e) Zoned cassiterite included in early wolframite. (f) Scheelite included in late wolframite. (g) Complexely zoned fluorite included in quartz. (h) Native bismuth (Bi) and quartz included in galena (Gl). (i) Zaravistskite (Zar) partially surrounding native bismuth and included in late arsenopyrite (Ars). (j) Oscillatory zoned early arsenopyrite included in quartz. (k) Early arsenopyrite included in pyrite (Py). (l) Chalcopyrite (Chp), quartz and late pyrite included in late arsenopyrite. (m) Sphalerite (Sph) partially surrounded and penetrated by late arsenopyrite. (n) Native bismuth included in cosalite (Cos) and both included in molybdenite (Mo). (o) Native bismuth included in bismuthinite (Bis).

Fig. 7 - Metallographic textures of the main ore minerals at the Carris mine. (a) Wolframite (W) plus cassiterite (Cst) and scheelite (Sch). (b) Scheelite (dark grey) replacing wolframite (main phase- lighter grey) along clivages. (c) Later subhedral arsenopyrite (Ars) surrounding pyrite (Py) associated with quartz (Q). (d) Molybdenite (Mo), pyrite (Py), arsenopyrite (Ars) in association with an intergrowth of native bismuth and cosalite (Cos).

Fig. 8- Mineral paragenetic chart at the Carris W-Mo-Sn vein orebody.

Fig. 9- Fe *versus* Mg diagram of chlorite of the W-Mo-Sn quartz veins from Carris, northern Portugal showing that in zoned crystals in BSE images the lighter zone is richer in Fe and poorer in Mg than the darker zone and the unzoned crystals have an intermediate composition closer to that of the lighter zone.

Fig. 10- Compositional plots for wolframite of the W-Mo-Sn quartz veins from Carris, northern Portugal. (a) Mn vs Fe^{2+} showing that the earlier crystals are the richer in Mn. (b) Plot of $(Nb^{5+} + Fe^{3+}_{cal})$ versus $(W^{6+} + Fe^{2+}_{cal} + Mn^{2+})$ for wolframite crystals containing Nb.

Fig. 11- Compositions of arsenopyrite and pyrite of the W-Mo-Sn quartz veins from Carris, northern Portugal. (a) S-Fe-As diagram showing the positions of diagrams (b) and (c) for

arsenopyrite and (d) for pyrite. (b) In zoned arsenopyrite grains, the lighter zone in BSE images is richer in As content and poorer in S content that the darker zone. (c) No distinction in chemical composition occurs between the early and younger arsenopyrites. (d) The lighter pyrite in BSE images is richer in As content than the common pyrite.

Fig. 12- Fluid inclusions from ore minerals at the Carris W-Mo-Sn mine: (a) Intragranular trail of pseudosecondary fluid inclusions with aqueous carbonic fluid. (b) Typical triphasic aqueous carbonic fluid inclusions from the same sample. (c) Trail of low salinity aqueous fluid inclusions in quartz associated with wolframite. (d) Group of Lw fluid inclusions in scheelite. (e) Isolated Lw fluid inclusion in beryl. (f) Lw fluid inclusions in fluorite. Bar = 20 μm.

Fig. 13- Histogram of the homogenization temperatures (Th) observed in microthermometry of the fluid inclusions from Carris orebody.

Fig. 14- Salinity *vs.* temperature of homogenization (Th) for fluid inclusions from the Carris mine.

Fig. 15- Raman peak for the aqueous carbonic fluid inclusion shown inside the box.

Fig. 16- $^{40}Ar^*/^{4}He$ *vs.* $^{3}He/^{4}He$ (*Ra*) plot of inclusion-trapped fluids from the Carris tungsten-molybdenum-tin deposit. $^{40}Ar^*$ is non-atmospheric argon, i.e. $^{40}Ar^* = {}^{40}Ar - 295.9\ {}^{36}Ar$.

Fig. 17- P-T estimates for deposition at Carris orebody. P-T area for episyenitization from Jaques et al., 2010. Vertical dashed lines- median and average value of Th for the aqueous carbonic fluids (280º) and average temperature for aqueous fluids in scheelite (266ºC); horizontal dashed line- pressure corresponding to the intersection of the Th = 280ºC and the higher isochore for the aqueous carbonic fluids; Isochores: 1- Lc-w fluids in quartz associated with wolframite deposition, 2-5 Lw fluids in scheelite, quartz, beryl and fluorite, respectively.

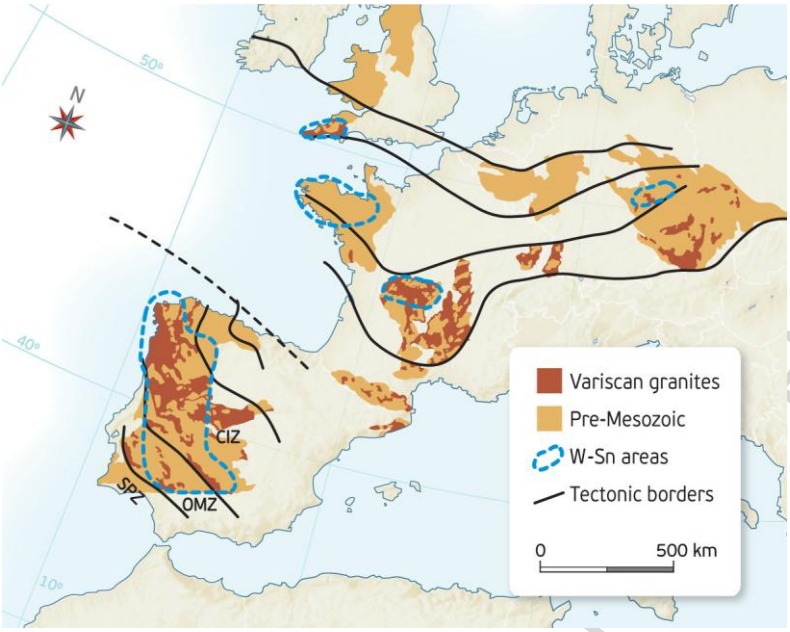

Figure 1

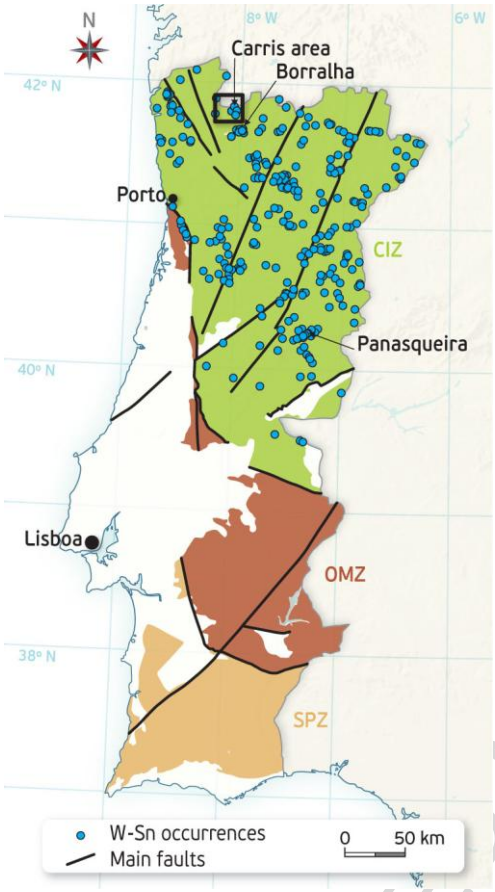

Figure 2a

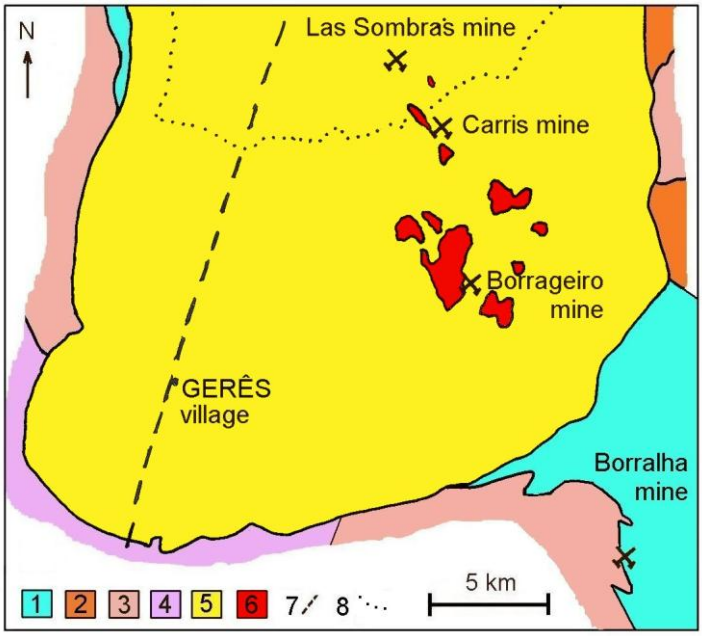

Figure 2b

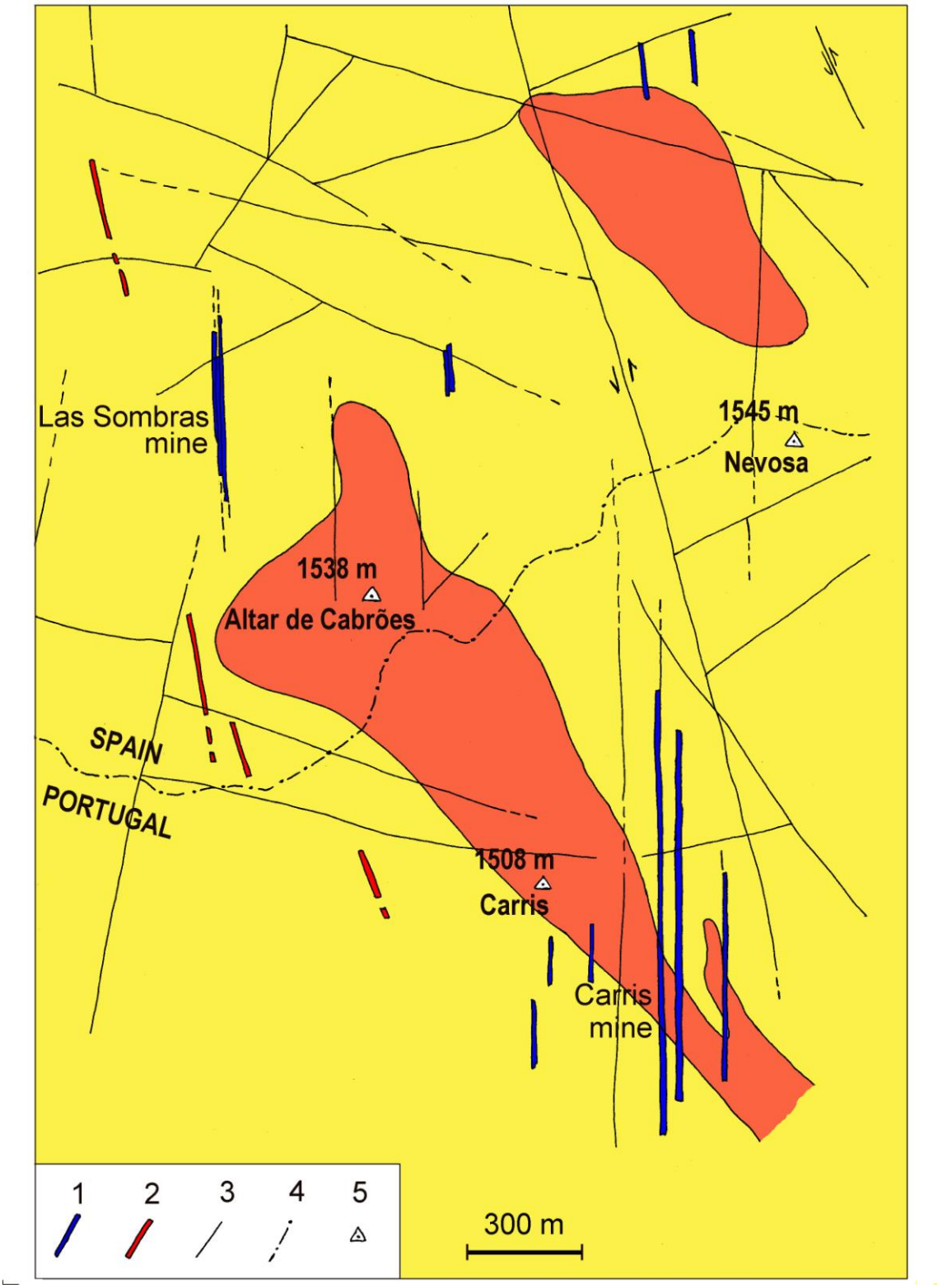

Figure 3

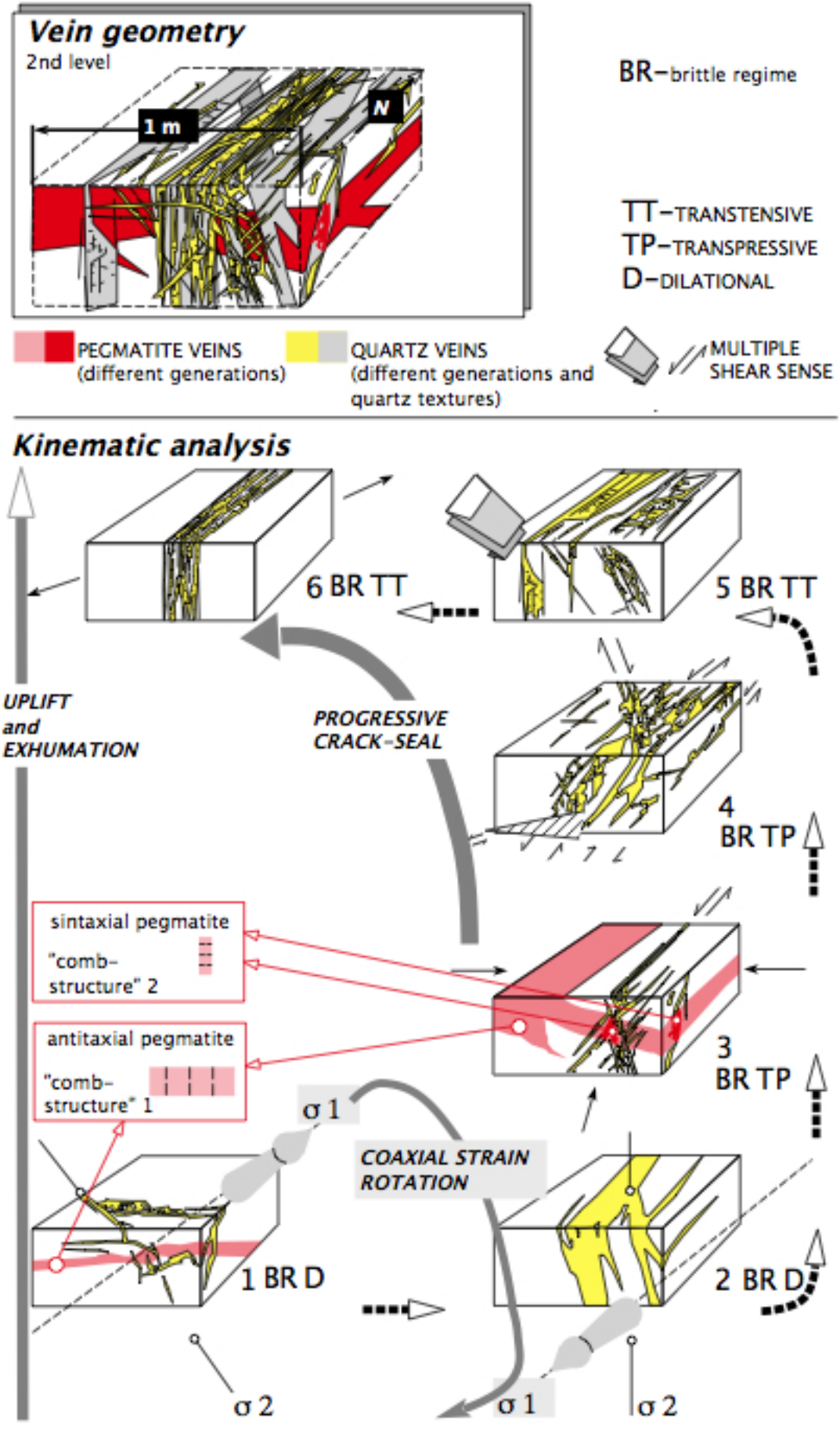

Figure 4

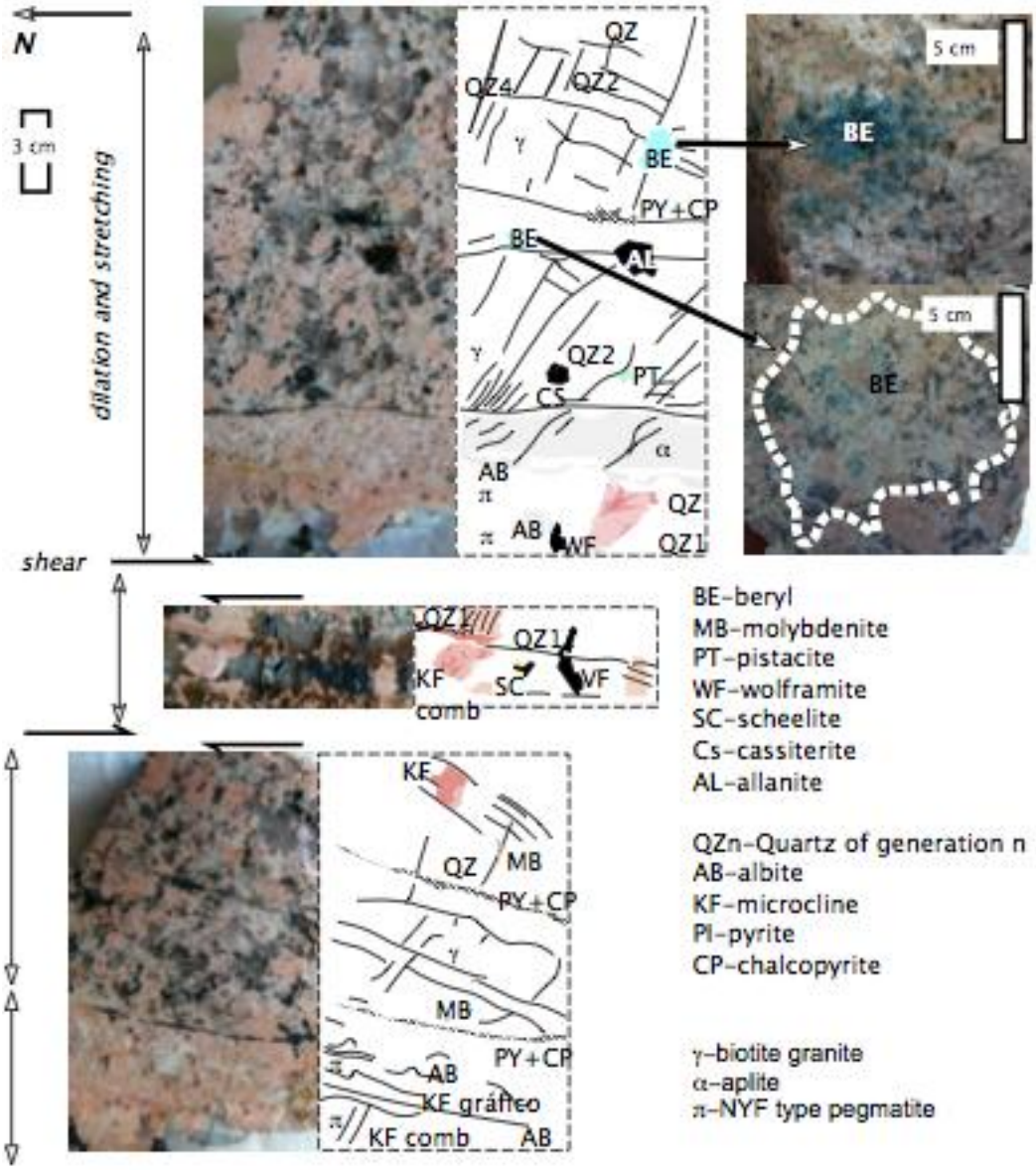
N
3 cm
dilation and stretching
shear
QZ
QZ4
QZ2
γ
BE
PY+CP
AL
QZ2
PT
CS
α
AB
π
QZ
QZ1
WF
5 cm
BE
5 cm
BE
QZ1
QZ1
KF
comb
SC
WF
KF
QZ
MB
PY+CP
γ
MB
PY+CP
AB
KF gráfico
KF comb
AB
BE-beryl
MB-molybdenite
PT-pistacite
WF-wolframite
SC-scheelite
Cs-cassiterite
AL-allanite
QZn-Quartz of generation n
AB-albite
KF-microcline
PI-pyrite
CP-chalcopyrite
γ-biotite granite
α-aplite
π-NYF type pegmatite

Figure 5

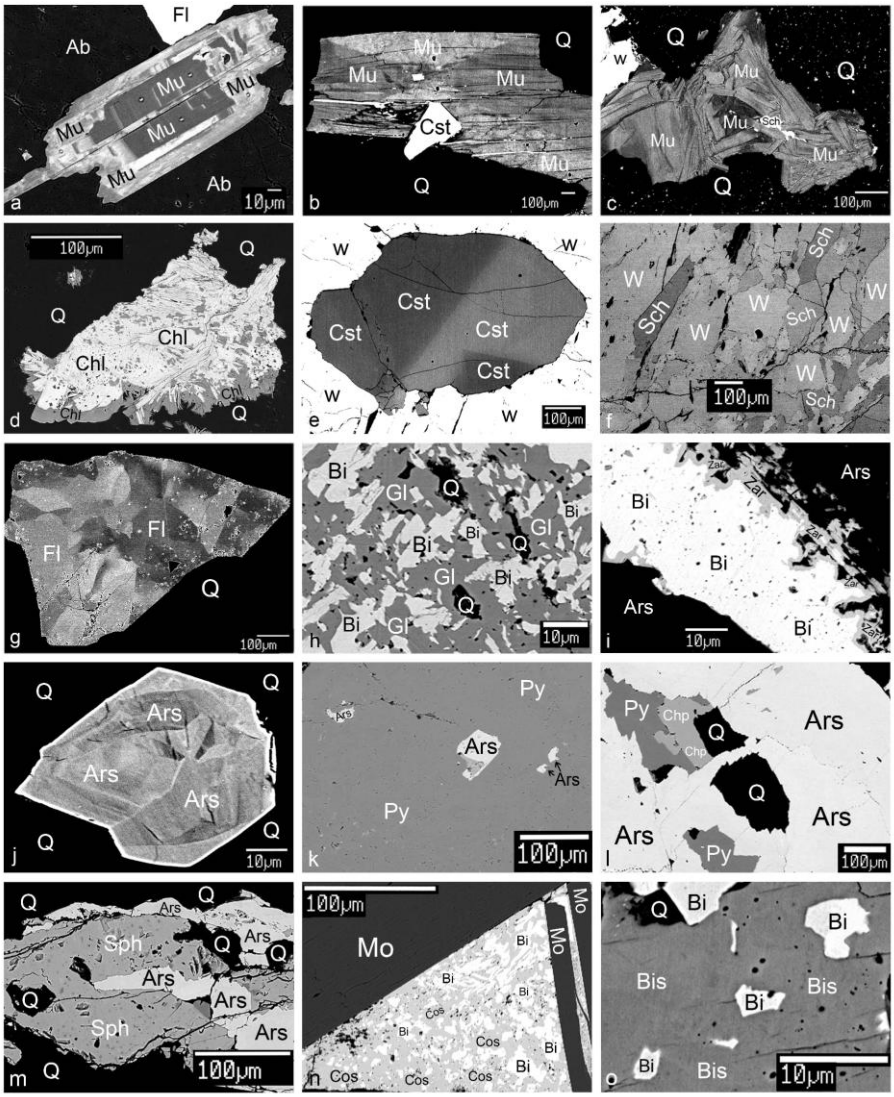

Figure 6

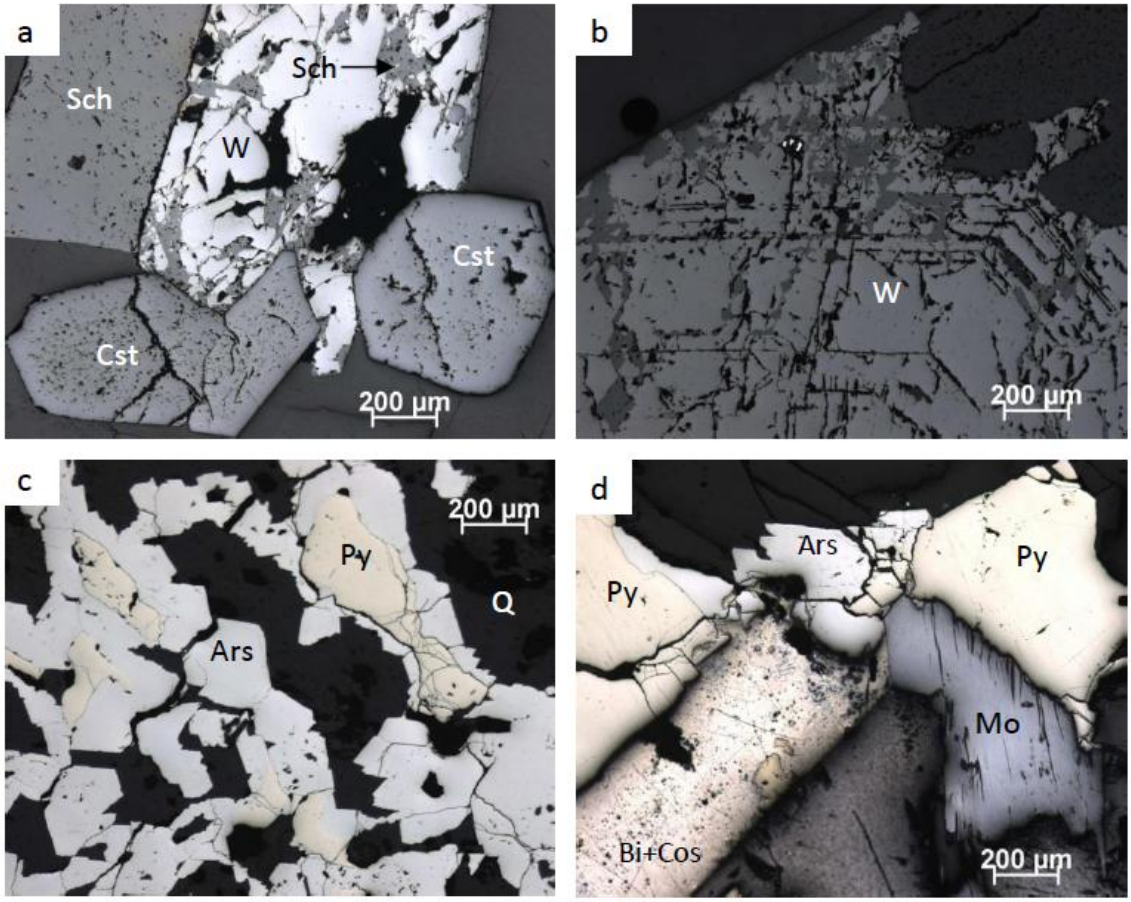

Figure 7

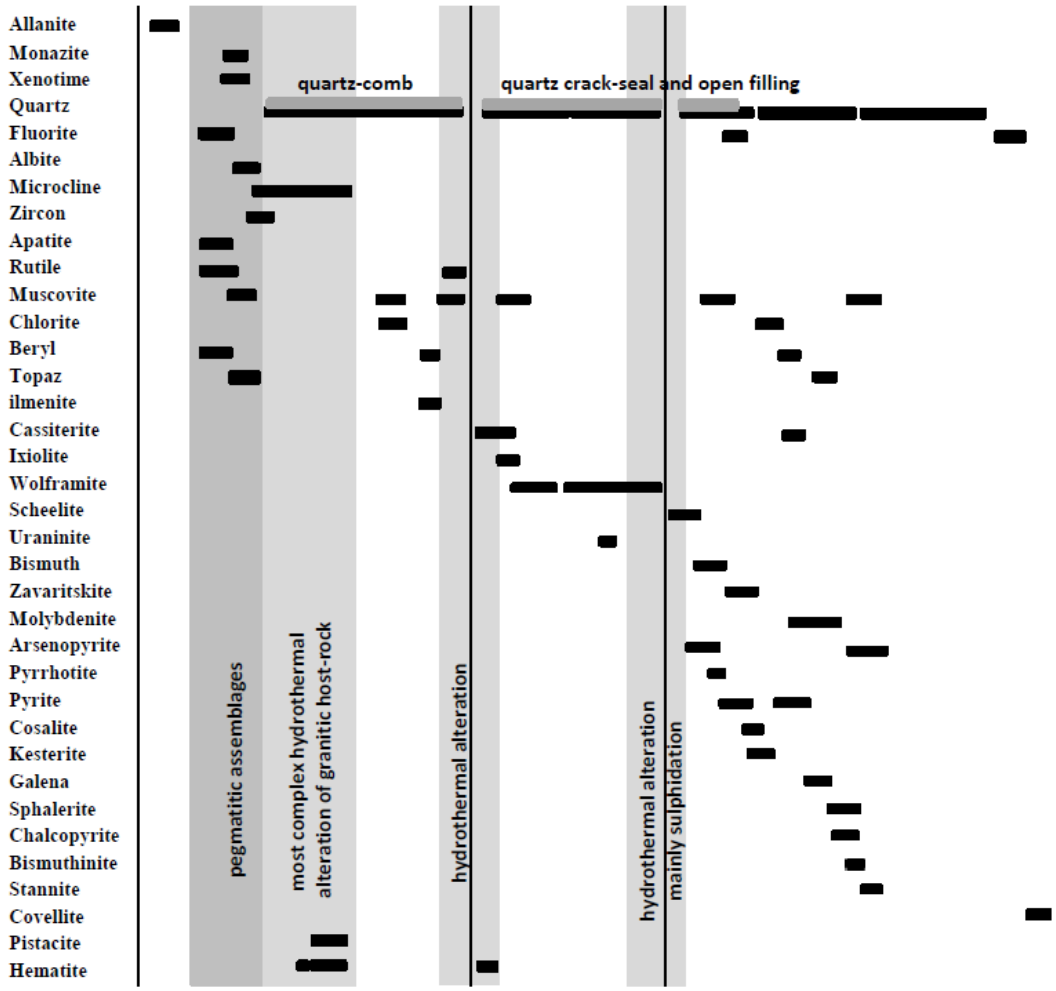

Figure 8

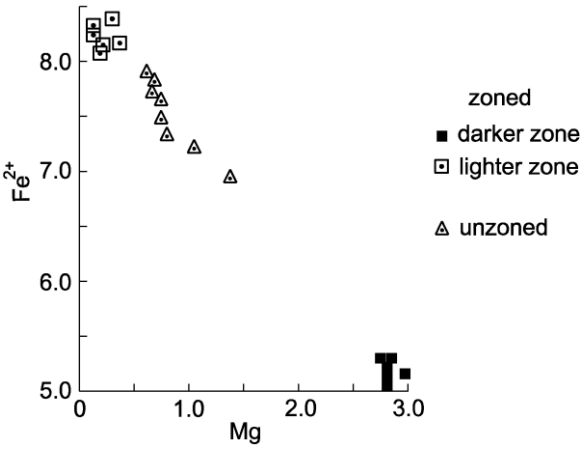

Figure 9

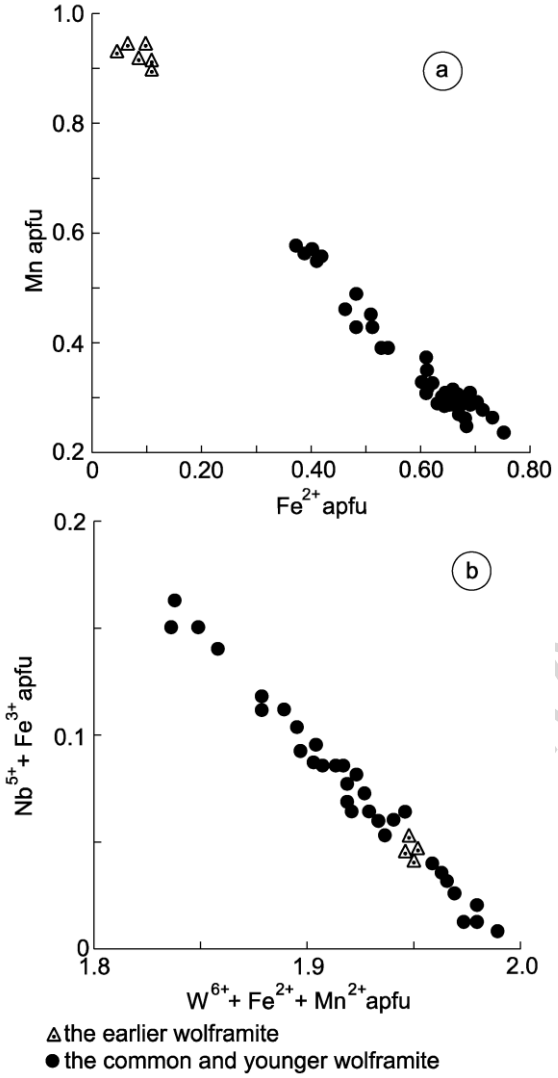

Figure 10

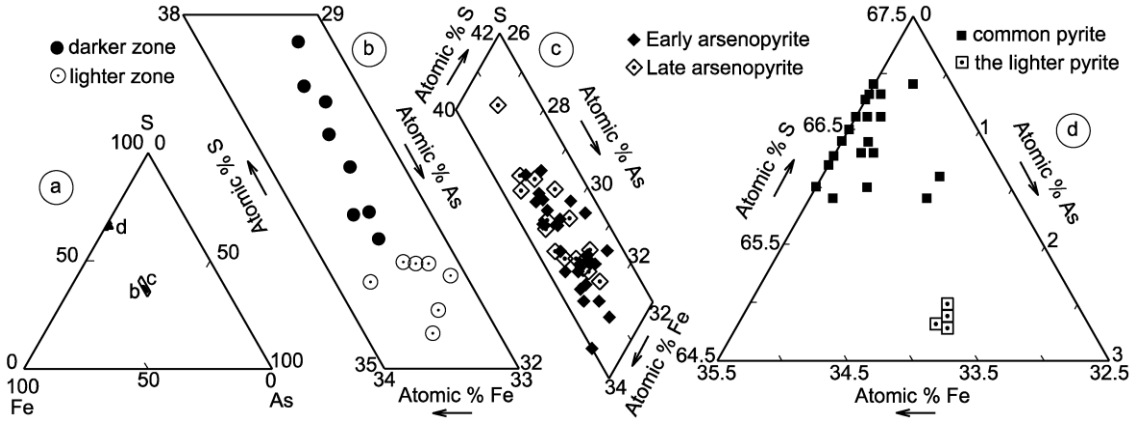

Figure 11

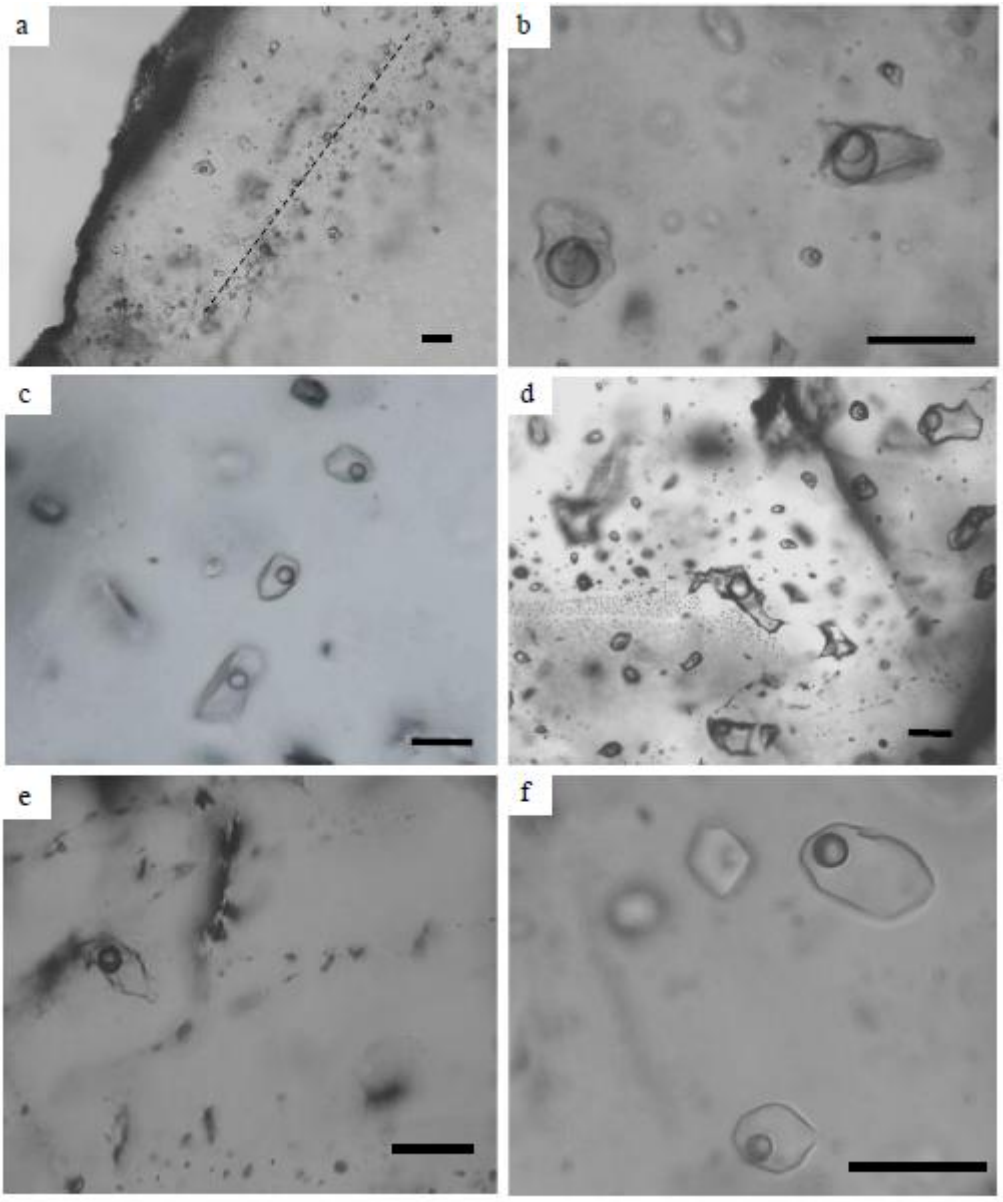

Figure 12

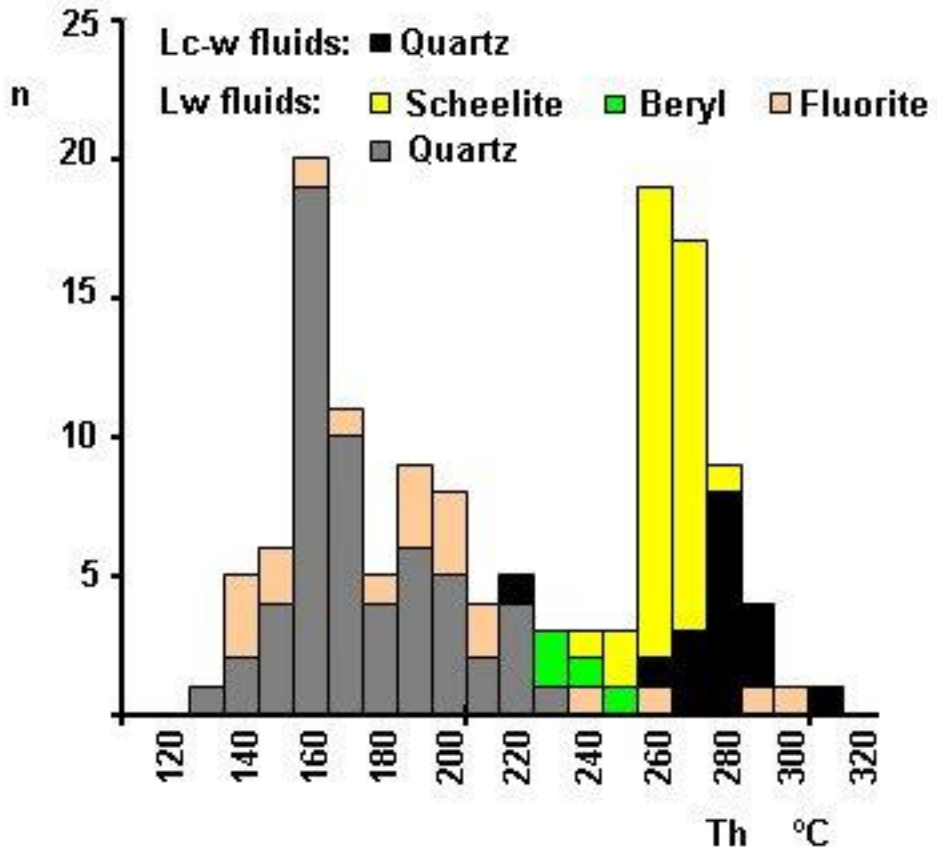

Figure 13

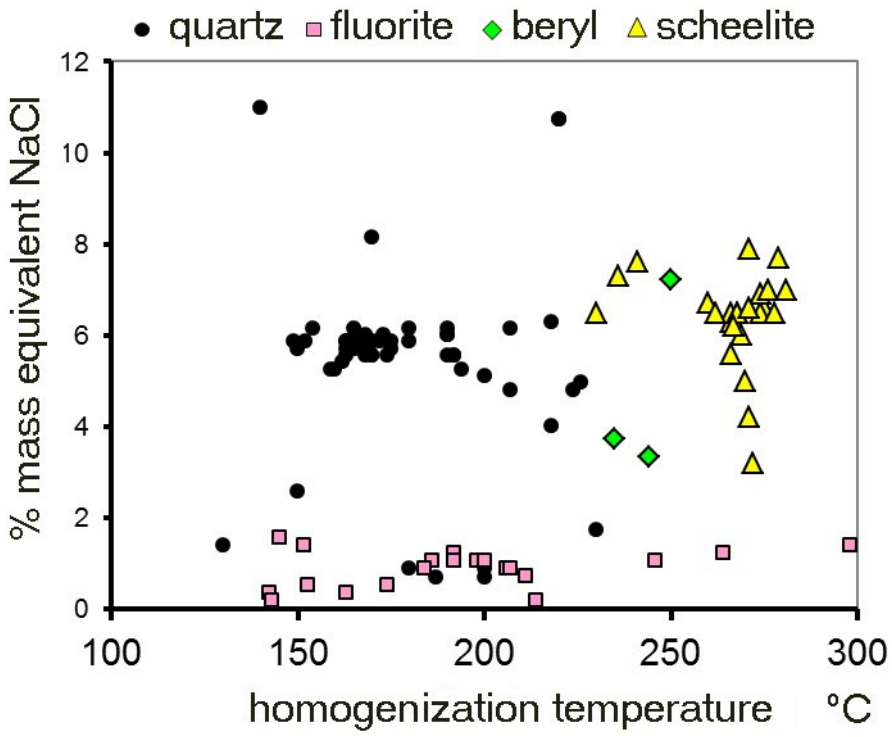

Figure 14

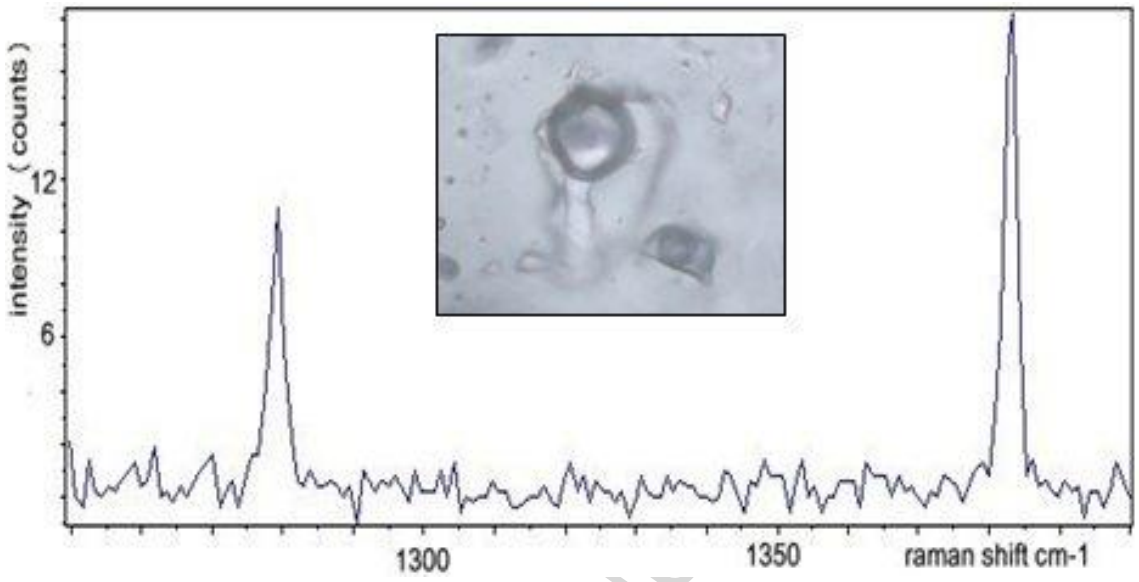

Figure 15

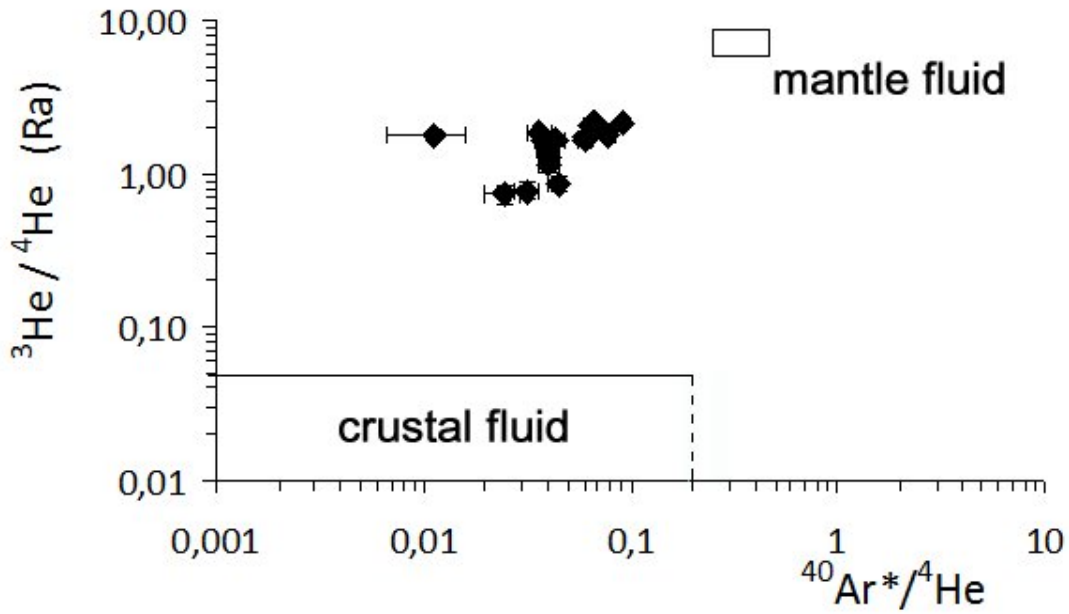

Figure 16

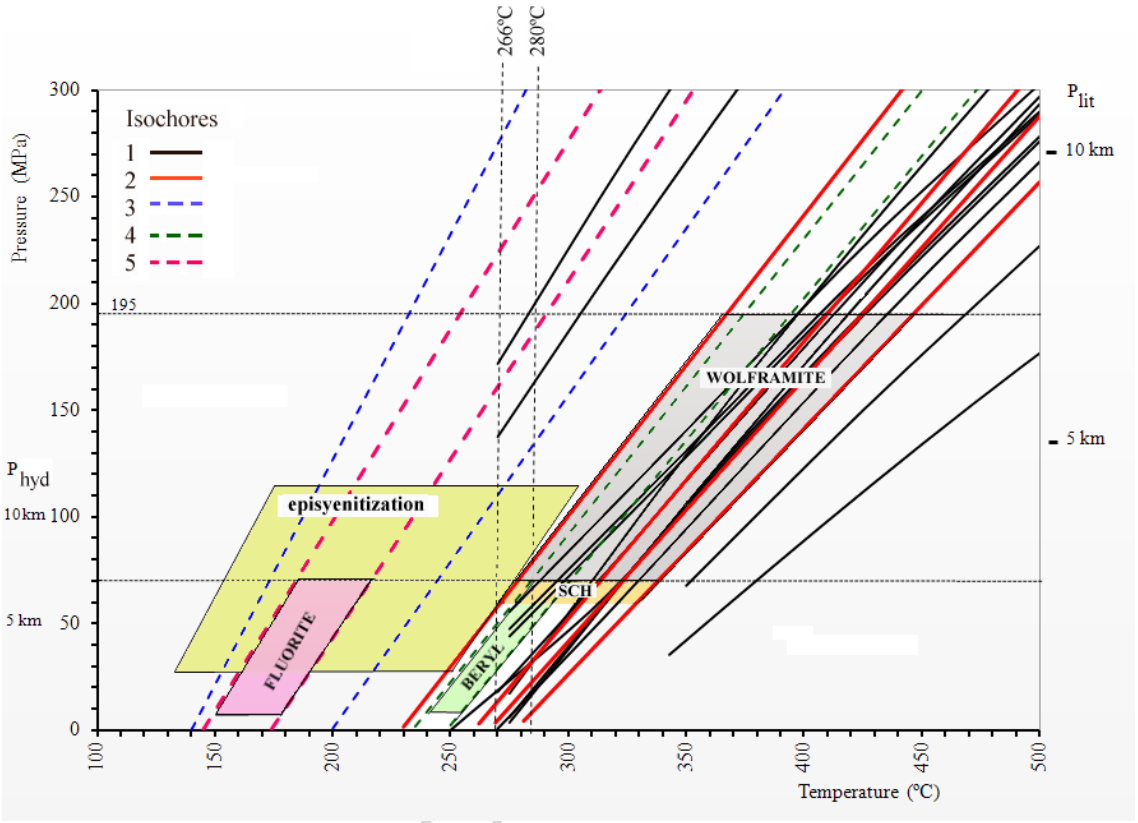

Figure 17

Graphical Abstract

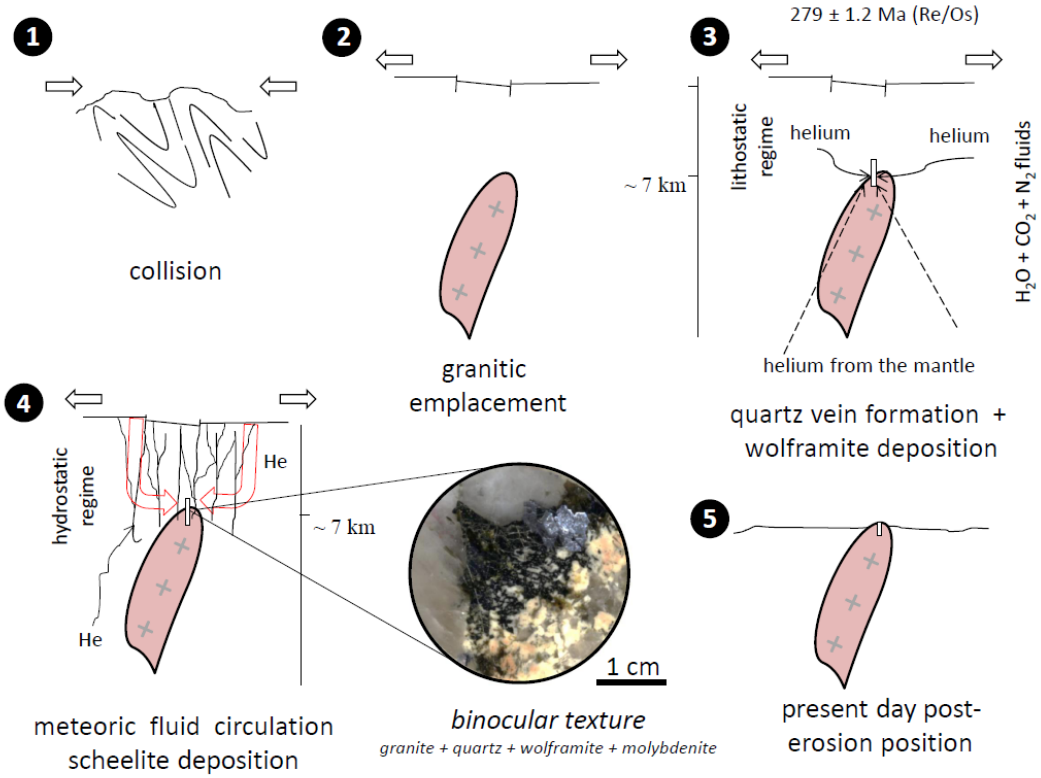

Table 1
Mineralogy of the tungsten-molybdenum-tin quartz veins from Carris, northern Portugal

Mineral	Grain size	Shape	Abundance	Contact relationships and comments
Monazite	Fine	Euhedral	Very rare	Included in quartz, microcline and apatite
Xenotime	Fine	Euhedral	Very rare	Included in quartz
Quartz	Coarse	Subhedral to anhedral	Dominant	Six generations: 1) close to feldspars and muscovite; associated with: 2) cassiterite and earlier wolframite; 3) later wolframite; 4) scheelite; 5) sulfides; 6) later fluorite
Fluorite	Fine	Subhedral	Rare	Three generations: 1) in miarolitic cavities; 2) included in albite (Fig. 6a), quartz, K-feldspar; 3) later than sulphides and sulphosalts
Albite	Coarse	Euhedral to subhedral	Small amounts	Included in quartz and microcline at the veins walls
Microcline	Coarse	Euhedral to subhedral	Small amounts	Close to the vein walls
Zircon	Fine	Euhedral	Rare	Included in muscovite
Apatite	Fine	Euhedral to subhedral	Rare	Included in muscovite
Rutile	Fine to medium	Subhedral	Rare	Two generations included in: 1) muscovite, 2) cassiterite
Muscovite	Coarse	Subhedral and radial	Frequent	Six generations: 1) included in albite (Fig. 6a); 2) intergrowth with chlorite; 3) included in quartz; 4) partially surrounding cassiterite (Fig. 6b); 5) surrounding wolframite and scheelite (Fig. 6c); 6) surrounding sulphides
Chlorite	Fine	Subhedral to anhedral	Rare	Included in quartz (Fig. 6d), intergrown with muscovite and partially surrounding it
Cassiterite	Medium	Euhedral to subhedral	Frequent	Two generations: 1) subhedral included in quartz and wolframite (Fig. 6e); 2) very small anhedral crystals of cassiterite (8-195 μm) surrounded by covellite in veinlets also containing chalcopyrite and cutting kesterite

Ixiolite	Fine	Euhedral	Very rare	Included in wolframite and scheelite
Wolframite	Coarse	Euhedral to subhedral	Dominant	Two generations: 1) with inclusions of cassiterite (Fig. 6e); 2) partially replaced by scheelite (Fig. 6f)
Scheelite	Medium	Subhedral	Frequent	In general surrounds and replaces wolframite
Uraninite	Fine	Subhedral	Very rare	Partially surrounded by muscovite and pyrite
Native bismuth	Coarse	Subhedral	Frequent	Penetrates wolframite and is included in galena, late arsenopyrite (Fig. 6h, i) and molybdenite
Zavaritskite	Fine	Subhedral	Rare	Partially surrounding native bismuth (Fig. 6i)
Arsenopyrite	Medium to fine	Euhedral, subhedral, later anhedral	Frequent	Two generations: 1) included in quartz, pyrite (Fig. 6j, k) and sphalerite; 2) later arsenopyrite partially surrounding pyrite (Fig. 6l) and containing inclusions of galena
Pyrite	Medium	Subhedral to anhedral	Small amount	Two generations: 1) surrounding arsenopyrite (Fig. 6k); 2) included in later arsenopyrite (Fig. 6l)
Cosalite	Medium	Anhedral	Rare	With inclusions of native bismuth (Fig. 6n), included in later pyrite
Galena	Fine	Anhedral	Rare	Included in sphalerite
Sphalerite	Fine	Anhedral	Rare	With inclusions of galena exsolved in chalcopyrite as blebs; surrounding arsenopyrite and penetrating pyrite; partially surrounded and penetrated by late arsenopyrite (Fig. 6m)
Chalcopyrite	Fine	Anhedral	Rare	With inclusions of fluorite; included in late arsenopyrite (Fig. 6l)
Molybdenite	Coarse	Euhedral	Abundant	Included in quartz, surrounding cassiterite, wolframite, native bismuth and cosalite; with inclusions of native bismuth and cosalite (Fig. 6n)
Bismuthinite	Fine	Anhedral	Rare	With inclusions of native bismuth (Fig. 6o)
Kesterite	Fine to medium	Anhedral	Rare	Included in quartz
Ilmenite	Fine	Subhedral	Rare	Included in the earlier cassiterite
Pistacite	Fine	Subhedral	Rare	Related to microclinization, pre-dating the main episodes of veining, or cementing quartz-feldspar cataclasis,

				in fault gouges
Table 1 (continuation)				
Mineralogy of the tungsten-molybdenum-tin quartz veins from Carris, northern Portugal				
Mineral	Grain size	Shape	Abundance	Contact relationships and comments
Hematite	Very fine to fine	Subhedral	Small amount	Associated with microclinization or, later on, related to cryptocrystalline deposition of silica (jasper)
Allanite	Fine	Euhedral to anhedral	Rare	As an accessory mineral of metasomatized granite or included in the most typical pegmatite assemblages
Beryl	Medium to coarse	Subhedral	Small amounts	Early pegmatitic to late miarolitic in host-granite gaps and, interstitial, in replenishment sites related to early stages of shear
Topaz	Fine to coarse	Euhedral to anhedral	Rare	Early pegmatite or metasomatic (locally as by-product of phylic, host-granite, hydrothermal alteration) to late miarolitic in dilation sites, inside quartz veins
Stannite	Fine to medium	Anhedral	Rare	Included in quartz

Table 2
Compositions of feldspars of the W-Mo-Sn quartz veins from Carris

Albite	An mol%	wt% P_2O_5	wt% SrO	wt% BaO	wt% Rb_2O	wt% Cs_2O
	0-1.0	0-0.02	≤ 0.06-0.26	≤ 0.06	≤ 0.06	≤ 0.06
Microcline	Or content mol%					
	97.1-98.4	0-0.03	≤ 0.06-0.17	≤ 0.06-0.18	≤ 0.06-0.14	≤ 0.06

An - anorthite content; microperthitic microcline with a triclinicity ($\triangle = 12.5\,(d_{131} - d_{1\bar{3}1})$ = 0.83); Or – orthoclase.

Table 3
Electron microprobe chemical analyses in wt% of muscovite of W-Mo-Sn quartz veins from Carris, northern Portugal

Muscovite	1				2		3				4			
	Included in albite				Intergrown with chlorite		Included in quartz				Surrounding cassiterite			
	DZ	σ	LZ	σ	Mean	σ	DZ	σ	LZ	σ	DZ	σ	LZ	σ
SiO_2	45.79	0.29	46.39	0.13	49.01	0.31	49.93	0.12	45.60	0.22	46.57	0.20	45.17	0.38
TiO_2	0.03	0.02	0.24	0.12	0.05	0.02	0.06	0.01	0.47	0.05	0.34	0.02	0.43	0.07
Al_2O_3	37.61	0.55	31.56	0.71	32.67	0.23	30.91	0.10	28.66	0.47	30.28	0.10	28.37	0.53
FeO	0.54	0.17	4.63	0.32	1.56	0.05	2.30	0.14	6.41	0.06	4.55	0.17	6.91	0.58
MnO	0.12	0.10	0.19	0.07	—	—	0.10	0.03	0.25	0.02	0.14	0.06	0.30	0.07
MgO	—	—	0.65	0.41	1.00	0.04	1.11	0.02	1.46	0.10	1.36	0.08	1.61	0.11
ZnO	0.01	0.01	0.05	0.04	0.03	0.03	0.06	0.05	0.09	0.05	0.11	0.12	0.02	0.03
Li_2O*	0.03	0.01	0.01	—	0.20	0.01	0.24	0.01	1.32	0.13	0.81	0.19	1.39	0.16
CaO	0.04	0.02	0.01	0.01	0.05	—	0.03	0.01	—	—	0.01	0.01	0.01	0.02
BaO	0.12	0.02	0.29	0.02	0.04	0.03	0.03	0.01	0.07	0.02	0.07	0.04	0.06	0.04
Na_2O	0.51	0.02	0.29	0.03	0.04	—	0.03	0.02	0.25	0.01	0.34	0.03	0.26	0.04
K_2O	10.60	0.08	10.65	0.11	10.62	0.21	10.35	0.10	10.72	0.10	10.44	0.14	10.37	0.11
Rb_2O	0.11	0.03	0.15	0.01	0.13	0.03	0.11	0.05	0.18	0.02	0.15	0.03	0.15	0.03
Cs_2O	—	—	0.01	0.02	0.03	0.01	0.02	0.01	0.05	0.02	0.02	0.03	0.03	0.01

F	0.40	0.06	0.79	0.04	0.59	0.02	0.69	0.03	2.49	0.19	1.71	0.30	2.59	0.23
H_2O**	4.34	0.02	4.03	0.04	4.24	—	4.18	0.02	3.19	0.10	3.60	0.14	3.12	0.13
	100.25		99.94		100.26		100.15		101.21		100.50		100.79	
O≡ F	0.17		0.33		0.25		0.29		1.05		0.72		1.09	
Total	100.08		99.61		100.01		99.86		100.16		99.78		99.70	
Si	3.030	0.023	3.156	0.011	3.248	0.012	3.319	0.009	3.131	0.013	3.164	0.016	3.118	0.013
Al^{IV}	0.970	0.023	0.844	0.011	0.752	0.012	0.681	0.009	0.869	0.013	0.836	0.016	0.882	0.013
Σ	4.000		4.000		4.000		4.000		4.000		4.000		4.000	
Al^{VI}	1.963	0.016	1.686	0.045	1.799	0.011	1.740	0.003	1.450	0.020	1.589	0.005	1.429	0.041
Ti	0.001	0.001	0.012	0.006	0.002	0.001	0.003	—	0.024	0.003	0.017	0.001	0.022	0.004
Fe^{2+}	0.030	0.009	0.263	0.019	0.086	0.003	0.128	0.008	0.368	0.005	0.259	0.009	0.399	0.034
Mn	0.007	0.006	0.011	0.004	—	—	0.006	0.001	0.015	0.002	0.008	0.004	0.017	0.004
Mg	—	—	0.066	0.042	0.099	0.003	0.110	0.002	0.149	0.011	0.137	0.008	0.166	0.011
Zn	—	0.001	0.002	0.002	0.001	0.001	0.003	0.003	0.005	0.003	0.006	0.006	0.001	0.001
Li	0.031	0.001	0.079	0.006	0.052	0.002	0.064	0.004	0.364	0.037	0.219	0.052	0.386	0.046
Σ	2.030		2.120		2.040		2.050		2.380		2.240		2.420	
Ca	0.002	0.001	0.001	—	0.004	—	0.002	0.001	—	—	0.001	0.001	0.001	0.002
Ba	0.001	0.001	—	0.001	0.001	0.001	0.001	—	0.002	0.001	0.002	0.001	0.002	0.001
Na	0.065	0.003	0.038	0.003	0.005	—	0.004	0.002	0.033	0.001	0.045	0.004	0.035	0.006

K	0.895	0.006	0.924	0.013	0.898	0.016	0.878	0.008	0.939	0.009	0.905	0.010	0.913	0.009
Rb	0.005	0.001	0.007	0.001	0.006	0.001	0.005	0.002	0.008	0.001	0.007	0.001	0.007	0.001
Cs	—	—	—	0.001	0.001	—	0.001	—	0.001	0.001	0.001	0.001	0.001	—
Σ	0.970		0.970		0.920		0.891		0.983		0.961		0.960	
F	0.084	0.012	0.170	0.009	0.124	0.004	0.145	0.006	0.541	0.041	0.367	0.065	0.565	0.052
OH*	1.916	0.012	1.830	0.009	1.876	0.004	1.855	0.006	1.459	0.041	1.633	0.065	1.435	0.052
n	8		8		8		6		6		8		8	

Table 3 (continuation)
Electron microprobe chemical analyses in wt% of muscovite of W-Mo-Sn quartz veins from Carris, northern Portugal

Muscovite	5				6			
	Surrounding wolframite and scheelite				Surrounding pyrite			
	DZ	σ	LZ	σ	DZ	σ	LZ	σ
SiO_2	48.90	0.66	46.34	0.51	46.72	0.23	45.37	0.20
TiO_2	0.05	0.03	0.24	0.06	0.03	0.03	0.22	0.19
Al_2O_3	31.85	0.79	29.45	0.50	30.22	0.50	27.74	0.27
FeO	2.48	0.41	5.78	0.30	5.35	0.39	7.33	0.28
MnO	0.05	0.05	0.31	0.05	0.22	0.08	0.30	0.05
MgO	0.69	0.08	1.31	0.12	0.85	0.30	1.97	1.04
ZnO	0.04	0.04	0.02	0.05	0.04	0.08	—	—
Li_2O*	0.24	0.04	0.49	0.11	0.32	0.07	1.18	0.04
CaO	0.03	0.02	0.01	0.02	—	—	0.01	0.01
BaO	0.05	0.04	0.06	0.04	0.13	0.02	0.10	0.12
Na_2O	0.03	0.02	0.08	0.02	0.14	0.03	0.18	0.03
K_2O	10.55	0.10	10.83	0.21	11.10	0.10	10.70	0.12
Rb_2O	0.14	0.04	0.17	0.02	0.19	0.06	0.22	0.02

Cs_2O	0.01	0.01	0.04	0.04	0.01	0.02	0.02	0.02
F	0.68	0.09	1.09	0.08	0.86	0.15	2.31	0.05
H_2O**	4.17	0.13	3.85	0.05	3.98	0.07	3.24	0.03
	99.96		100.07		100.16		100.89	
O≡F	0.29		0.46		0.36		0.97	
Total	99.67		99.61		99.80		99.92	
Si	3.266	0.036	3.183	0.030	3.196	0.011	3.140	0.007
Al^{IV}	0.734	0.036	0.817	0.030	0.804	0.011	0.860	0.007
Σ	4.000		4.000		4.000		4.000	
Al^{VI}	1.773	0.031	1.567	0.011	1.632	0.036	1.401	0.015
Ti	0.003	0.002	0.012	0.003	0.002	0.002	0.012	0.010
Fe^{2+}	0.139	0.023	0.332	0.019	0.306	0.023	0.424	0.018
Mn	0.003	0.003	0.018	0.003	0.013	0.005	0.018	0.003
Mg	0.069	0.007	0.134	0.012	0.086	0.030	0.203	0.011
Zn	0.002	0.002	0.001	0.003	0.002	0.004	—	—
Li	0.063	0.011	0.122	0.012	0.089	0.020	0.330	0.010
Σ	2.050		2.190		2.130		2.390	
Ca	0.002	0.002	0.001	0.001	—	—	0.001	0.001
Ba	0.001	0.001	0.001	0.001	—	—	0.003	0.003
Na	0.004	0.003	0.011	0.003	0.019	0.004	0.024	0.004
K	0.899	0.011	0.949	0.013	0.968	0.007	0.946	0.009
Rb	0.006	0.002	0.008	0.001	0.009	0.002	0.010	0.001
Cs	—	—	0.001	0.001	—	0.001	—	0.001
Σ	0.910		0.970		1.000		0.980	
F	0.144	0.019	0.237	0.018	0.186	0.032	0.505	0.011
OH*	1.856	0.019	1.763	0.018	1.814	0.032	1.495	0.011
n	6		6		6		6	

Cl was not detected. DZ – darker zone, LZ – lighter zone in BSE images. — Not detected. Calculated number of ions on the basis of 12 oxygen atoms, Li_2O* values calculated from the equation of Tischendorff et al. (1997), OH* – calculated by difference to 2.0, H_2O** – calculated by stoichiometry. n – number of analysis.

Table 4
Electron microprobe chemical analyses in wt% of chlorite of W-Mo-Sn quartz veins from Carris, northern Portugal

	Zoned				Unzoned	
	darker zone		lighter zone			
	Mean	σ	Mean	σ	Mean	σ
SiO_2	26.38	0.26	23.58	0.24	23.82	0.33
TiO_2	0.01	0.02	0.01	0.02	0.03	0.03
Al_2O_3	21.85	0.30	20.56	0.34	20.84	0.41
FeO	28.74	0.48	42.54	0.62	39.46	1.32
MnO	1.64	0.22	1.21	0.37	0.82	0.56
MgO	8.81	0.25	0.67	0.28	2.38	0.68
CaO	0.02	0.02	0.01	0.02	0.02	0.02
Na_2O	0.04	0.03	0.04	0.02	0.02	0.02
K_2O	0.01	0.01	0.01	0.01	0.07	0.07
F	—	—	0.18	0.20	0.31	0.08
	87.50		88.81		87.77	
O≡F	—		0.08		0.13	
Total	87.50		88.73		87.64	
Si	5.681	0.025	5.436	0.072	5.451	0.073
Al^{IV}	2.319	0.025	2.564	0.072	2.549	0.073
Σ	8.000	—	8.000	8.000	8.000	8.000
Al^{VI}	3.226	0.081	3.022	0.087	3.073	0.108
Ti	0.002	0.002	0.002	0.003	0.005	0.006
Fe^{2+}	5.176	0.069	8.201	0.118	7.552	0.293
Mn	0.299	0.039	0.236	0.071	0.159	0.106
Mg	2.828	0.084	0.230	0.095	0.812	0.219
Ca	0.005	0.004	0.002	0.003	0.005	0.004

Na	0.017	0.012	0.018	0.008	0.009	0.011
K	0.003	0.003	0.003	0.003	0.020	0.020
Σ	11.5600		11.7100		11.6400	
F	—	—	0.131	0.143	0.224	0.057
n	6		6		11	

σ – Standard deviation; — not detected; n – number of analyses. Calculated number of ions on the basis of 28 oxygen atoms.

Table 5
Electron microprobe chemical analyses in wt% of oxide minerals of W-Mo-Sn quartz veins from Carris, northern Portugal

	Rutile included in		Ilmenite included in	Cassiterite		Ixiolite		Wolframite			Scheelite		Uraninite
	muscovite	cassiterite	cassiterite	Earlier	Younger			Earlier	Common				
TiO_2	96.28	73.51	52.41	0.36	—	2.77	TiO_2	0.02	—	MnO	0.01	UO_2	87.65
SnO_2	0.15	1.66	1.11	99.57	99.96	2.01	MnO	21.60	6.06	CaO	20.12	FeO	0.13
Nb_2O_5	0.69	9.85	0.35	0.02	—	50.81	Fe_2O_3	1.26	1.02	WO_3	79.33	PbO	3.94
Ta_2O_5	—	9.63	0.05	0.03	—	2.03	FeO	1.09	16.71	MoO_3	0.15	Er_2O_3	0.04
WO_3	1.69	0.06	0.04	0.18	—	19.09	Nb_2O_5	0.07	4.93	Total	99.61	ThO_2	6.42
FeO	1.44	4.78	44.96	0.05	0.14	6.35	SnO	—	0.32			La_2O_3	0.14
MnO	0.07	0.04	1.34	0.01	—	10.29	Ta_2O_5	—	0.28			Y_2O_3	0.69
Sc_2O_3	—	—	—	—	—	6.46	WO_3	75.88	70.77			Ce_2O_3	0.35
	100.32	99.53	100.26	100.22	100.10	99.81		99.92	100.09				99.36
Ti	0.97	0.82	1.99	0.0		0.16	Ti	0.0		M		U	0.8

	7	7	6	07	—	4		01	—	n	—		88
Nb	0.004	0.067	0.008	—	—	1.804	Mn	0.917	0.253	Ca	1.034	Fe	0.005
Ta	—	0.039	0.001	—	—	0.043	Fe^{3+}	0.048	0.038	W	0.986	Pb	0.048
Sn	0.001	0.010	0.011	0.990	1.000	0.063	Fe^{2+}	0.046	0.688	Mo	0.003	Er	0.001
W	0.006	—	—	0.001	—	0.388	Nb	0.002	0.109	Total	2.023	Th	0.066
Fe	0.016	0.060	1.905	0.001	0.003	0.417	Sn	—	0.006			La	0.002
Mn	0.001	0.001	0.079	—	—	0.685	Ta	—	0.004			Y	0.017
Sc	—	—	—	—	—	0.442	W	0.986	0.902			Ce	0.006
Total	1.005	1.004	4.000	0.999	1.003	4.006	Total	2.000	2.000			Σ	1.033
							mol%						
							Mn WO_4	90.8	25.8				

— Not detected. Cation formula of minerals based on number of atoms of oxygen; rutile, cassiterite and uraninite (2), ilmenite (6), ixiolite (8), wolframite (4) with the Fe^{3+}, Fe_2O_3 and FeO calculated on the basis of charge balance and 2 cations, scheelite (4). Wolframite: 1 – the earlier and richer in Mn content, 2 – the younger and richer in Fe^{2+} and Nb contents.

Table 6
Selected electron microprobe chemical analyses in wt% of sulfides and sulfosalt of W-Mo-Sn quartz veins from Carris, northern Portugal

	Ni	Co	Cu	Ag	Au	Zn	Fe	Mn	Cd	Sb	As	Bi	Pb	Mo	Sn	S	Total
Arsenopyrite																	
Darker zone	—	0.04	—	—	0.03	—	35.39	—	—	—	41.35	—	—	—	—	23.09	99.90
Lighter zone	—	0.06	—	—	0.07	—	35.30	—	—	—	43.01	—	—	—	—	21.56	100.00
Core	—	0.05	0.01	0.02	0.12	—	35.45	0.02	—	—	41.41	0.09	0.05	—	—	22.72	99.94
Rim	—	0.06	—	0.01	—	—	34.78	—	—	—	43.82	0.06	0.06	—	—	21.60	100.39
Pyrite																	
Common	—	0.05	—	0.02	—	—	46.90	—	—	—	—	—	—	—	—	52.87	99.84
Lighter	—	0.04	—	0.02	0.04	—	45.75	—	—	—	2.99	—	—	—	—	50.67	99.51
Cosalite	—	—	0.37	1.88	—	—	—	—	0.11	1.12	—	42.95	37.13	—	—	16.01	99.57
Galena	—	—	—	0.36	—	—	—	—	0.12	—	—	—	86.49	—	—	13.10	100.07
Sphalerite	—	—	—	—	0.02	59.34	5.70	0.07	1.46	—	0.06	—	—		—	33.19	99.84
Sphalerite	—	—	—	—	—	54.20	9.97	0.33	1.50	—	—	0.11	0.07		—	33.61	99.79
Chalcopyrite	—	0.01	34.62	0.04	—	—	30.15	0.01	—	—	0.02	0.17	—		—	34.90	99.92
Molybdenite	—	—	—	—	—	—	—	—	—	—	—	—	—	59.8	—	39.8	99.73

															9	4	
Bismuthinite	—	—	—	—	—	—	—	—	—	0.49	—	79.92	—	—	—	19.46	99.87
Stannite																	
Darker zone	—	—	29.10	0.06	—	4.73	9.48	—	—	—	—	—	—	—	26.60	29.96	99.93
Lighter zone	—	—	28.40	5.05	—	3.87	9.05	—	—	—	—	—	—	—	24.64	28.70	99.71
Kesterite	—	—	30.40	0.07	—	8.22	5.34	0.07	—	—	—	—	0.05	—	26.61	29.34	100.10

The minimum detection limit of all elements is 200 ppm. — Less than the minimum detection limit.

Table 7
Electron microprobe chemical analyses in wt% of halides and element from W>Mo>Sn quartz veins from Carris, northern Portugal

	Fluorite				Zavaritskite		Native bismuth	
	DZ	LZ	Unzoned		Unzoned			
Ca	51.78	51.52	50.35	Bi_2O_3	95.88		Bi	99.19
F	47.83	48.53	49.45	F	7.49		Sb	0.87
Total	99.61	100.05	99.80		103.37		Total	100.06
				O≡F	3.15			
Ca	1.000	1.000	1.000	Total	100.22			
F	1.948	1.980	2.070					
				Bi	1.011			
				F	0.968			

DZ – darker zone, LZ – lighter zone of the second generation. Unzoned – the first generation. Calculated number of ions on the basis of 1 Ca for fluorite and 2(O, F) for zavaritskite.

Table 8
Microthermometric data for fluid inclusions from the W-Mo-Sn quartz veins from Carris, northern Portugal.

Microthermometric data (ºC)												
Fluid type	Mineral	Flw (Flc)	$TmCO_2$	n	Tm_{ice}	n	TmCl	n	$ThCO_2$	n	Th	n
Lc-w	Quartz	0.8 (0.5-0.8)	-58.3 / -57.0 (-57.6)	21	n.o.		7.2 / 10.1 (8.5)	14	21.4 / 25.5 23.0 / 26.1 (24.2)	L 7 V 13	226 / 310 [280]	16
Lw	Quartz	0.8 / 0.9	-		-7.4 / -0.1 (-3.4)	134	-		-		130 / 230 [160]	42
Lw	Beryl	0.8	-		-3.7 / -0.1 (-1.9)	7	-		-		235 / 250 [242]	4
Lw	Fluorite	0.7 / 0.9	-		-0.9 / -0.1 (-0.5)	21	-		-		142 / 306 [190]	20
Lw	Scheelite	0.9	-		-5.0 / -0.9	33	-		-		230 / 281 (266)	35

(...) average value; [...] mode value. Flw: degree of filling; Flc: liquid CO_2/total CO_2; $TmCO_2$: melting temperature of CO_2; Tm_{ice}: final ice melting temperature; TmCl: melting temperature of clathrates; $ThCO_2$- homogenization temperature of the CO_2 phase; Th: total homogenization temperature. n: number of measurements. First melting of ice was always between -25ºC and -21ºC.

Table 9

Bulk composition and density for aqueous carbonic and aqueous fluid inclusions from quartz, scheelite, beryl and fluorite of the Carris W-Mo-Sn ore, northern Portugal

		Bulk fluid composition (mole %)					density
	inclusion	XH_2O	XCO_2	XN_2	XNa^+	XCl^-	gcm^{-3}
	R3	82.75	14.76	1.33	0.58	0.58	0.95
	S1	84.39	12.51	1.94	0.58	0.58	0.92
	R4	85.59	12.53	1.50	0.19	0.19	0.91
	S4	82.54	6.68	0.28	5.25	5.25	0.87
	C2	77.38	12.27	0.15	5.10	5.10	0.86
Aqueous	S2	78.26	11.39	0.39	4.98	4.98	0.85
carbonic	S3	84.84	5.26	0.10	4.90	4.90	0.85
fluid	C1	79.55	10.95	0.46	4.52	4.52	0.84
inclusions	R1	93.22	4.22	0.36	1.10	1.10	0.83
	C3	91.47	4.38	0.13	2.01	2.01	0.83
	C4	85.52	4.57	0.05	4.93	4.93	0.82
	R6	92.70	6.63	0.59	0.04	0.04	0.78
	R5	91.17	6.88	0.25	0.85	0.85	0.77
	R2	87.65	5.27	0.16	3.46	3.46	0.74
	Q3	98.92	-	-	0.54	0.54	0.84
	Q4	99.56	-	-	0.22	0.22	0.87
Aqueous	Q2	99.14	-	-	0.43	0.43	0.95
fluid	Q1	92.94	-	-	3.53	3.53	0.99
inclusions	Be-1	98.09	-	-	0.96	0.96	0.83
	Be-2	96.21	-	-	1.90	1.90	0.86
	FL-1	99.78	-	-	0.11	0.11	0.93
	FL-2	99.35	-	-	0.32	0.32	0.89
	SCH-1	95.00	-	-	2.50	2.50	0.86
	SCH-2	97.98	-	-	1.01	1.01	0.86

Obs. All the aqueous carbonic fluid inclusion was studied in quartz. Abbreviations on the inclusion column, means the mineral were fluids were studied: quartz (Q), beryl (Be), fluorite (FL) and scheelite (SCH).

Table 10
Rhenium – Osmium isotopic data and ages for molybdenites from the Carris W-Mo-Sn quartz veins (PV-1) and Gerês granite (PG-1), northern Portugal

Sample	^{187}Os ppb	^{187}Re ppb	Re ppm	Age (Ma)	± 2σ
PV-1	0.3872 ± 0.0007	83.26 ± 0.20	0.1325 ± 0.0003	**278.5**	**1.2**
PG-1	1.1661 ± 0.0017	249.1 ± 0.6	0.3964 ± 0.0009	**280.3**	**1.2**

Table 11

He-Ar isotope data for pyrite from the Carris mine

Sample	Crushing number	Weights a (g)	4Heb (10-7 cm3 STP)	40Arb (10-8 cm3 STP)	3He/4He (Ra)	40Ar/36Ar	3He/36Ar	4He (cm3 STP/g)	40Ar (cm3 STP/g)
c1	1		2.64±0.05	13.3±0.17	1.12±0.03	321.40±6.27	0.0010		
	2		2.18±0.04	3.48±0.04	1.46±0.04	393.42±24.60	0.0050		
	total	0.1357	4.82±0.13	16.80±0.30	1.28±0.05	334.06±21.88	0.0017	3.55E-06	1.24E-06
c4	1		2.42±0.04	9.17±0.05	2.17±0.05	388.94±10.52	0.0031		
	2		1.67±0.03	3.56±0.02	1.82±0.05	356.26±15.43	0.0043		
	total	0.126	4.09±0.09	12.74±0.11	2.03±0.07	379.21±19.36	0.0035	3.25E-06	1.01E-06
c2	1	0.1604	1.51±0.02	6.27±0.04	1.80±0.06	364.23±10.52	0.0022	9.43E-07	3.91E-07
c3	1		2.91±0.04	9.94±0.06	2.15±0.06	368.27±6.82	0.0032		
	2		1.27±0.02	2.88±0.02	2.05±0.07	410.18±21.80	0.0052		
	total	0.1616	4.18±0.09	12.82±0.11	2.12±0.09	376.91±21.22	0.0036	2.58E-06	7.93E-07
l1a	1		1.27±0.02	10.91±0.06	1.63±0.06	317.71±5.52	0.0008		
	2		1.74±0.03	11.11±0.06	1.74±0.06	326.83±6.35	0.0012		
	total	0.161	3.01±0.07	22.03±0.18	1.69±0.08	322.25±8.40	0.0010	1.87E-06	1.37E-06
l1b	1		2.24±0.03	11.46±0.07	0.86±0.02	323.66±5.03	0.0008		
	2		3.79±0.06	8.90±0.05	0.73±0.02	329.87±5.48	0.0014		
	total	0.1628	6.03±0.13	20.35±0.17	0.78±0.03	326.34±7.42	0.0011	3.70E-06	1.25E-06
l2a	1		3.95±0.06	11.02±0.06	1.65±0.04	351.00±5.45	0.0029		

2		0.82±0.01	5.54±0.03	1.76±0.05	300.53±6.99	0.0011		
total	0.1525	4.77±0.10	16.56±0.14	1.67±0.06	332.33±9.29	0.0022	3.13E-06	1.09E-06

a. Sample weights are the <100 μm fraction after crushing.

b. Errors are at the 1σ confidence level; totals are the sums of all crushes.

Highlights

- We study a W-Sn-Mo Variscan quartz vein system in Portugal (Iberian W-Sn province)
- Re-Os dating of molybdenite yield ages of 279 ± 1.2 Ma.
- Helium and argon isotopes indicate a mixture of a crustal and mantle derived-fluid
- Pressure oscillations, P-T decrease and mixing are the main causes for W deposition